Physics of Fluids

Experimental investigation of single bubbles rising in stagnant liquid: Statistical analysis and image processing

Cite as: Phys. Fluids **33**, 103611 (2021); https://doi.org/10.1063/5.0061581
Submitted: 28 June 2021 • Accepted: 27 September 2021 • Published Online: 19 October 2021

Ida K. Kure, Hugo A. Jakobsen, Nicolas La Forgia, et al.

Physics of Fluids ARTICLE scitation.org/journal/phf

Experimental investigation of single bubbles rising in stagnant liquid: Statistical analysis and image processing

Cite as: Phys. Fluids **33**, 103611 (2021); doi: 10.1063/5.0061581
Submitted: 28 June 2021 · Accepted: 27 September 2021 ·
Published Online: 19 October 2021

Ida K. Kure,[a] Hugo A. Jakobsen, Nicolas La Forgia, and Jannike Solsvik[b]

AFFILIATIONS

Department of Chemical Engineering, Norwegian University of Science and Technology (NTNU), N-7491 Trondheim, Norway

[a]Author to whom correspondence should be addressed: ida.k.kure@ntnu.no
[b]Electronic mail: jannike.solsvik@ntnu.no

ABSTRACT

Despite the large effort devoted to the study of single bubbles rising in a stagnant liquid, the complex phenomena involved have resulted in a large scatter in the terminal velocity. Providing new experimental data where the statistical uncertainty is thoroughly evaluated is therefore necessary. Single bubble experiments were conducted in a tall vertical column containing stagnant liquid at ambient conditions. To track the bubbles over the spatial range, high-speed cameras were mounted on a linear unit drive. The tall column allowed us to study the effect of hydrostatic pressure and late developed bubble dynamics on the bubble motion. The bubble properties, i.e., the bubble velocity, size, shape, and trajectory, were evaluated using an image analysis processing method. The analysis includes a quantitative evaluation of important parameters involved in the handling of the raw data. Several of the existing correlations for the terminal velocity were validated against the experimental data. The data are well predicted by the correlation proposed by Tomiyama *et al.* ["Terminal velocity of single bubbles in surface tension force dominant regime," Int. J. Multiphase Flow **28**, 1497–1519 (2002)]. The uncertainty in the experimental data has been emphasized, providing a quantitative evaluation based on several statistical methods. The number of experimental events necessary to obtain statistical significance was evaluated using a 95% confidence interval. Satisfying precision is found to be fulfilled for 10–15 bubble rise events. For bubbles of comparable size, the statistically significant terminal velocity data were found to exhibit a small scatter.

I. INTRODUCTION

Many industrial processes involve gas–liquid interactions, including systems such as chemical reactors (e.g., bubble column, slurry column),[1–3] biochemical reactors (e.g., stirred tanks),[4,5] distillation, fermentation, waste-water treatment, nuclear engineering,[6,7] and metallurgical bubble column reactors.[8]

Interfacial heat and mass transfer are important phenomena involved in gas–liquid systems, and these phenomena are largely affected by key properties such as the bubble size, shape, trajectory, and velocity. Although most industrial processes concerning gas–liquid interactions involve swarms of bubbles, the understanding of a single bubble phenomenon is crucial as it serves as a basis for more complex multiple bubble systems. A common approach in single bubble experiments is to inject a volume of gas into a stagnant continuous phase and determine the bubble properties after steady conditions are attained. The terminal velocity, i.e., the steady bubble rise velocity, is an important property associated with the analysis of bubbles. It is included as an approximation in dimensionless groups such as the bubble Reynolds number (Re_b) and the Weber number. Moreover, the terminal velocity is embedded in the steady drag coefficient. Accurate mathematical models predicting the terminal velocity are thus of great importance from a process design point of view.

A. Literature review: Terminal velocity of single bubbles

A variety of theoretical and experimental studies exist on freely rising single bubbles.[9–26] Spherical bubbles at $Re_b < 1$ can be evaluated based on the theory of Stokes[9] or Hadamard[11]–Rybczynski.[12] The model by Stokes[9] is applicable for contaminated systems, whereas the model by Hadamard[11]–Rybczynski[12] can be employed for clean systems. The terminal velocity of large spherical cap bubbles can be evaluated by the correlation of Davies and Taylor.[27] Recent models on the terminal velocity include the correlation proposed by Baz-Rodrígues

et al.,[23] and the correlation by Tomiyama *et al.*[18] given as a function of the bubble aspect ratio.

An overview of early experimental data on the terminal velocity of air bubbles in water is provided in the textbook of Clift *et al.*[28] The terminal velocities presented by Clift *et al.*[28] reveal a large scatter in the literature values. Generally, the large scatter in the terminal velocities has been attributed to the presence of surfactants, which accumulate on the bubble surface and influence the bubble properties.[28–30] While the presence of surfactants in the continuous phase has been shown to result in a decreasing bubble rise velocity for smaller bubbles ($d_b < 1.34$ mm),[29] the bubble rise velocities obtained in an ultra-pure water system are reported to be constant and attain higher values compared to what is obtained in a contaminated system.[22,31,32]

More recently, the large scatter in the terminal velocity data has been attributed to the influence of the method of bubble formation.[18,19] In the studies of Tomiyama *et al.*,[18] Okawa *et al.*,[19] Celata *et al.*,[21] and Liu *et al.*[25] bubbles were produced with small and large bubble shape deformations by changing the inner diameter of the bubble formation device. The bubbles produced with initially large bubble shape deformations were found to attain higher terminal velocities compared to the bubbles produced with initially small bubble shape deformations. Tomiyama *et al.*[18] observed a tendency toward a zigzag bubble rise path when the bubbles were produced with initially small bubble shape deformations, whereas initially large bubble shape deformations were found to enhance the transition from a zigzag to a helical bubble rise path.

Experimental data on the terminal velocity have commonly been obtained in vertical columns with a limited spatial range. A summary of the column geometries employed in previous studies are provided in Table I, where the majority have been performed in limited column heights. Except in the work by Merker *et al.*,[33] all the cameras reported in Table I were restricted to a fixed position. Merker *et al.*[33] designed a traverse system at which two high-speed cameras were attached to continuously record the bubbles during the bubble ascent. The two high-speed cameras provided a three-dimensional view of the bubble shape and trajectory. Most of the studies reported in Table I have employed one camera (one-sided image acquisition), where the bubble size has been calculated from the projected area using the bubble axes. In some cases, an additional camera has been employed for several experimental runs to validate the calculated bubble diameter, shape, and trajectory based on the one-sided image recordings.[21,25] In pure water, Celata *et al.*[21] found the difference in the volume equivalent bubble diameter based on image acquisition from two sides of the bubble to be 0.3%. Okawa *et al.*[19] and Liu *et al.*[25] found the calculated bubble diameter obtained by employing one- and two-high speed cameras to agree within an error of $\pm 10\%$.

The main results from several experimental works on bubble velocity, size, shape, and trajectory are summarized in Table II, including an overview of the reported statistical and image analysis. The statistical analysis is commonly limited to reporting on the uncertainties without further discussion on the obtained statistics or providing a description of the uncertainty calculation approach. While few studies are providing the statistics along with the statistical methodology employed,[20] in some studies the experimental uncertainty is absent.[22,32] Except from a stepwise description of the conversion from an original to a binary image in the work of Liu *et al.*,[24] the image analysis and processing reported in the studies in Table II are found limited.

B. Novel contribution

Limited studies on single bubbles exist where both the method of bubble formation is known and in which a detailed statistical analysis is provided. Commonly, the average value along with the standard deviation is given without a quantitative discussion on the uncertainty. A large number of experimental data on the terminal velocity have been provided in the last decades in the studies of Tomiyama *et al.*,[18] Okawa *et al.*,[19] Celata *et al.*,[21] Celata *et al.*,[20] and Liu *et al.*[25] The terminal velocities reported by Tomiyama *et al.*,[18] Okawa *et al.*,[19] Celata *et al.*,[21] and Celata *et al.*[20] represent individual bubble measurements, and not statistical averages. Except from the more detailed description of the uncertainty given by Celata *et al.*,[20] the analysis is commonly limited to reporting the final values of the error.

Employing an image acquisition technique, such as in the previously presented studies,[14,15,18–22,24,25,29] is an advantage due to the method being non-intrusive. Despite the large application of the image acquisition technique, evaluation of the statistical uncertainty associated with image processing and analysis is limited to more recent work. A minimal discussion is found on the choice of threshold values used in the image analysis and the influence of the threshold on the calculated data. Commonly, only the applied value of the threshold is reported in the literature.

Experimental data acquisition is often very time-consuming. The statistical validity is often attributed and limited to the number of experiments. Regardless of this, few studies are found to attempt defining the minimal number of experimental events needed to obtain statistical significance.

This paper will provide new experimental data on the terminal velocity of single air bubbles in stagnant water at ambient temperature, in which it is explicitly reported on the method of bubble formation. The reported values will be average values calculated based on several single bubble events. A thorough evaluation will be given on the statistical uncertainty in the experimental data. The evaluation will be based on several statistical methods. Additionally, an evaluation will be given on the number of necessary bubble events to ensure data of statistical significance.

Unlike most previous studies, an experimental facility with the ability to continuously track the bubble was constructed in this study to generate experimental data of a rising bubble over a long vertical distance. The design and control of the dynamic facility will enable rapid changes in the mechanical parts involved, adapting to the transient motion of the bubble. High-resolution image acquisition over a longer vertical distance allows for investigation of potentially late developed bubble dynamics, in addition to the influence of the hydrostatic pressure. Contributing to the limited literature, a detailed description will be outlined on the system control of the dynamic facility.

The image processing method will be described in detail. The choice of important parameters influencing the calculated quantities will be emphasized. Such an important parameter is the threshold value used in the binarization of the original images. A sensitivity analysis will be given in which the bubble velocity and size are calculated considering several threshold values.

TABLE I. A summary of the experimental setups applied in previous publications.

Reference	Column	Camera setup	Bubble formation	Bubble diameter (mm)	Gas	Liquid	Temperature	Measured quantity
Aybers and Tapucu[29]	$17 \times 17 \times 100\,cm^3$	One camera, partly movable	Glass capillary	0.8–7.1	Air	Water	18 °C–39.1 °C	Bubble size, velocity, trajectory, shape
Duineveld[31]	$50 \times 50 \times 50\,cm^3$	One camera, fixed	···	0.7–1.9	Air	Ultrapure water ($\geq$ 18 MΩ cm)	19.6 ± 0.2 °C	Bubble size, velocity, shape
Wu and Gharib[32]	$15 \times 15 \times 61\,cm^3$	One camera, fixed	Glass capillary	1.0–2.1	Air	Deionized + distilled water, Ultrapure water ($\geq$ 18 MΩ cm)	22 ± 0.3 °C	Bubble size, velocity, path, shape
Tomiyama *et al.*[18]	$10 \times 20 \times 20\,cm^3$	Two cameras, fixed	Nozzle	0.6–11	Air	Distilled water, distilled water w/ 0.000 75% soap	Ambient	Bubble size, velocity, trajectory, shape
Okawa *et al.*[19]	$25 \times 30 \times 40\,cm^3$	Two cameras, fixed	Glass and sst pipe	0.7–3.7	Air	Distilled water	15 °C–90 °C	Bubble size, velocity, shape
Celata *et al.*[21]	$10 \times 10 \times 30\,cm^3$	One camera, fixed	Nozzle	0.5–6	N_2	Distilled-, de-ionized-, tap water, pure FC-72	Ambient	Bubble size, velocity, trajectory, shape
Celata *et al.*[20]	$10 \times 10 \times 30\,cm^3$	One camera, fixed	Glass nozzle, orifice in flat brass	0.5–4	N_2	Deionized water, refrigerant FC-72	Ambient	Bubble size, velocity, shape
Liu *et al.*[25]	$15 \times 15 \times 50\,cm^3$	One camera, fixed	Sst nozzle, flat top	0.5–11	Air	Water, glycerin aqueous solution	8 °C–29 °C	Bubble size, velocity, trajectory, shape
Sanada *et al.*[22]	···	One camera, fixed	Orifice in nylon tube	0.4–1.7	N_2	Ultrapure water ($\geq$ 18 MΩ cm)	23 °C–25.4 °C	Bubble size, velocity, shape
Merker *et al.*[33]	$7.5 \times 200\,cm^2$	Two cameras, movable	Capillary	0.9–2.8	Air,	CO_2,NO	Ultrapure water (0.055μ S cm^{-1})	25 °C
Bubble size, velocity, trajectory, shape, mass transfer coefficient								
Current work	$4 \times 4 \times 200\,cm^3$	One camera, movable	Glass needle	0.8–1.9	Air	Deionized water	23±0.5°C	Bubble size, velocity, trajectory, shape

TABLE II. A summary of the main results from the studies in the literature review.

Reference	Main results	Image analysis	Statistical analysis
Tomiyama *et al.*[18]	Strong dependency between the initial bubble shape deformations, terminal velocity, and trajectory. Small initial bubble shape deformations resulted in low terminal velocity and high bubble aspect ratio. Initial small bubble shape deformations commonly result in a zigzag rise path. Large initial bubble shape deformations resulted in higher terminal velocities and lower bubble aspect ratio. Terminal velocity of contaminated bubbles agreed with clean bubbles with small initial shape deformations.	Illustrations of original and binarized images	Uncertainty in bubble velocity based on the spatial resolution of the images.
Okawa *et al.*[19]	At normal temperature, the bubble velocity and onset to path oscillations were affected by the method of formation. Bubbles with initial large shape deformations are well predicted by terminal velocity correlations for pure systems. Terminal velocity correlations for contaminated systems are suitable for bubbles with initial small shape deformations. At high temperatures, a dependency between the terminal velocity and the bubble formation method was observed.	No detailed description.	Velocity: estimated error ± 2 mm/s.
Celata *et al.*[21]	Large scatter in terminal velocity data for both pure and contaminated liquids. Large initial bubble shape deformations observed when the bubble diameter exceeded the nozzle diameter. Initial large bubble shape deformations resulted in higher terminal velocities than with initial small bubble shape deformations. Best model predictions: $d_b > 1.3$ mm: Tomiyama *et al.*[18] in both contaminated and pure water, $d_b < 1.3$ mm: Peebles and Garber[13] for pure water and Ishii and Chawla[34] for contaminated water.	No detailed description.	Bubble position: estimated error ± 0.1 mm Uncertainties: Terminal velocity: $\pm 5.2\%$, Bubble diameter: average error $\pm 5.2\%$, with values ranging from $\pm[3.4, 7.9]\%$. Bubble shape: mean error $\pm 10\%$ with values ranging from $\pm[7.0, 15.0]\%$.
Celata *et al.*[20]	Best model prediction for the terminal velocity given by the correlation of Tomiyama *et al.*[18] Model predictions found to exhibit an error up to $\pm 50\%$.	No detailed description.	Instantaneous bubble velocity: $\pm[1.7, 15.4]\%$, terminal velocity: $\pm[0.7, 2.0]\%$ (unknown if water or FC-72). Bubble diameter: $\pm 2.9\%$, ranging from $\pm[1.0, 11.0]\%$ in water, $\pm 4.3\%$, ranging from $\pm[2.0, 9.0]\%$ in FC-72. Bubble aspect ratio: $\pm 6.6\%$, ranging from $\pm[0.4, 20.0]\%$ in water, $\pm 6.2\%$, ranging from $\pm[0.6, 20.0]\%$ in FC-72.
Liu *et al.*[25]	Higher terminal velocity and lower bubble aspect ratio with helical rise path.		Uncertainties: Terminal velocity: $\pm[0.04, 4.65]\%$, bubble diameter: $\pm[2.0, 8.3]\%$ for $d_b \in (0.5, 1.0)$ mm, $\pm[1.6, 4.0]\%$ for $d_b \in (1.0, 2.5)$ mm.
Liu *et al.*[24]	Further evaluation of the data obtained by Liu *et al.*[25] Best model prediction: Tomiyama *et al.*[18] in water. Moreover, the data were well predicted by the proposed correlation of Ishii and Chawla.[34]	Description of the stepwise conversion from an original to a binary image.	

TABLE II. (Continued.)

Reference	Main results	Image analysis	Statistical analysis
Wu and Gharib[32]	Bubble shape, velocity, and rise path are influenced by the inner diameter of the capillary. Inner diameter of the capillary exceeding the bubble diameter resulted in lower terminal velocities than obtained when the bubble diameter exceeded the capillary inner diameter. Terminal velocity data for bubbles produced with direct injection of air (pinch-off method) coincided with the data obtained when the capillary inner diameter was smaller than the bubble diameter.	No description.	No statistical analysis.
Sanada *et al.*[22]	Critical bubble Reynolds number was found susceptible to the height of observation. The height of onset to path oscillations decreased for increasing bubble Reynolds number, while the height at which a terminal velocity was reached remained approximately unchanged. Discrepancy between the experimental data and the theoretical correlations for the bubble aspect ratio.	Limited discussion	No statistical analysis.

Finally, the accuracy of existing correlations for the terminal velocity will be assessed for bubbles in the size range $d_b \in [0.8, 1.9]$ mm. An attempt will be made to identify the most suitable correlation for the bubble shape, expressed in terms of dimensionless numbers.

II. BUBBLE HYDRODYNAMICS

A. Terminal velocity

A single bubble ascending in stagnant liquid rises under the influence of gravity. The main forces governing the bubble motion are buoyancy and drag. From the momentum balance formulation,[35] generally referred to as Newton's second law, the bubble velocity at which it rises can be determined:

$$\frac{d}{dt}(m_b v_b) = \rho_l g V_b - m_b g - \frac{1}{2}\rho_l C_D A_b^p |v_b| v_b + \dot{m} v_b S_b, \quad (1)$$

where m_b denotes the mass of the bubble, v_b the bubble velocity, ρ_l the liquid density, g the acceleration of gravity, V_b the bubble volume, C_D the drag coefficient, $A_b^p = S_b/4$ the projected area of the bubble, $S_b = \pi d_b^2$ the bubble surface, d_b the volume equivalent bubble diameter, and $\dot{m}$ the mass flux over the bubble interface. The LHS of (1) is the rate of change of linear momentum, the first and second terms on the RHS correspond to the body forces resulting from hydrostatic pressure and gravity, respectively, and the third term denotes the steady drag. Note that history-, lift-, and virtual mass forces have been neglected. The fourth term represents a source/sink term due to interfacial mass transfer. When there is net-zero transfer of mass across the bubble interface, $\dot{m} = 0$ and the fourth term vanishes.

When the buoyancy, gravity, and drag forces are balanced, a terminal velocity, v_T, is reached. By specifying the drag coefficient, the terminal velocity can be computed from the force balance in Eq. (2), or vice versa. It should be noted that the viscous and surface tension forces are implicitly expressed through the drag coefficient in Eq. (2),

$$v_T = \sqrt{\frac{4 d_b (\rho_l - \rho_g) g}{3 \rho_l C_D}}, \quad (2)$$

where ρ_g denotes the density of the gas.

The wake, which resides behind a rising bubble, plays an important role in the flow dynamics. When the relative velocity between an ascending bubble and the surrounding liquid is very low, the flow adjacent to the bubble will follow closely to the bubble surface. That is, for small bubble Reynolds numbers. As the bubble Reynolds number increases, the flow starts to separate from the bubble surface and the streamlines rejoin behind the bubble, forming a wake.[36] Determining the terminal velocity of an ascending bubble in a quiescent liquid is challenging due to the complex bubble dynamics and phenomena involved.

The terminal velocity is largely influenced by the bubble size, shape, and trajectory, the method of bubble formation, the fluid properties, and the degree of liquid contamination. A common approach when analyzing the terminal velocity is to distinguish between three regimes.[28] The regimes are: (1) the spherical regime ($d_b < 1$ mm), (2) the ellipsoidal regime (1 mm $< d_b <$ 18 mm), and (3) the spherical cap regime (18 $< d_b$ mm).

In the spherical regime (1), viscosity and buoyancy forces dominate the bubble motion. The bubbles are of spherical or close to a

spherical shape, the rise path is rectilinear, and the terminal velocity increases with increasing bubble size.

In the ellipsoidal regime (2), surface tension and inertia forces dominate the bubble motion. The bubble shape varies from the oblate ellipsoidal, spherical cap, or ellipsoidal-cap with surface wobbling. The terminal velocity may increase, stay constant, or decrease, depending on the bubble size. As the bubble size increases above $d_b = 1$ mm, a transition from a rectilinear to an oscillating rise path is observed. Here, the bubbles may take helical, zigzag, or rectilinear with rocking paths.[28] A wide scatter in available terminal velocity data is observed in the ellipsoidal regime.[18,28,36] Previously, the scatter has been attributed to the presence of surfactants. Surfactants in the continuous phase have been shown to significantly impact the bubble dynamics.[29,30,37] Frumkin and Levich[38] suggested the reduction in the terminal velocity with the presence of impurities to be explained by surfactant concentration gradients on the bubble surface, forming a stagnant cap (for illustration see, e.g., Alves *et al.*[30]). Surfactants in the front of the bubble are dragged to the rear end due to surface advection by the main flow. A surface tension gradient is formed, causing a tangential stress (the Marangoni effect), which opposes the viscous stress at the surface.[37] The surface mobility is affected, and the drag coefficient increases toward that of a rigid sphere.[30] Griffith[37] found the surface tension of smaller bubbles to cause the surface to become saturated. The saturation of the surface resulted in the bubble velocity decelerating more rapidly. Bubbles of size $d_b = 1.34$ mm reached a terminal velocity at which they rose for a longer time. Griffith[37] argued that the lack of negative effects of impurities on the terminal velocity of larger bubbles was due to their fast ascent. With a fast bubble ascent, the shearing forces on the bubble surface increase. As the shearing forces exceed the surface tension forces, impurities are not able to accumulate at the surface. More recently, Tomiyama *et al.*[18] and Okawa *et al.*[19] found scattering in the surface tension dominated regime to be caused by the bubble injection method, which influences the initial bubble shape deformation, the trajectory, and the terminal velocity. Tomiyama *et al.*[18] and Okawa *et al.*[19] observed bubbles with initially small bubble shape deformations to take a zigzag motion. On the contrary, large initial bubble shape deformations resulted in an enhanced transition from a zigzag to a helical rise path. Confirming the earlier observations by Saffman[39] and Ellingsen and Risso,[40] the transition from a zigzag to a helical path occurred, while the opposite was never observed. The bubbles formed with initial large shape deformations were found by Tomiyama *et al.*[18] and Okawa *et al.*[19] to take higher terminal velocities compared to the bubbles produced with initially small shape deformations. Wu and Gharib[32] and Liu *et al.*[25] reported on similar trends where higher terminal velocities were achieved when the bubbles were produced with initially large shape deformations compared to initially small shape deformations.

There is still no complete understanding of the phenomena causing the scattering in the terminal velocity data. At present, the scatter is attributed to either differences in the initial bubble shape deformations, concentration of surfactants, or wake evolution.[20,21]

In the spherical cap regime (3), the bubbles take spherical cap form, and the inertia- and buoyancy forces dominate the bubble motion. The terminal velocity is observed to increase with increasing bubble diameter. Despite the suggested limits separating the three regimes by Clift *et al.*,[28] there are no clear transition criteria in the literature.[20] Recently reported terminal velocity data by Liu *et al.*[24] are significantly different from the data obtained by Bryn,[41] Gorodetskaya,[42] Davies and Taylor,[43] and Napier *et al.*,[44] that are reported in the textbook of Clift *et al.*[28] Liu *et al.*[24] suggested that the differences in the observed regime limits are caused by the sensitivity of the terminal velocity to the bubble shape.

Several correlations have been proposed for the explicit computation of the terminal velocity. A summary of the proposed correlations is given in Table III. Stokes[9] and Hadamard[11]–Rybczynski[12] proposed correlations for spherical bubbles at $Re_b < 1$. The correlation by Stokes[9] is applicable for bubbles with immobile surfaces, while the correlation by Hadamard[11]–Rybczynski[12] is applicable for bubbles with mobile surfaces. Using boundary-layer theory, Levich[10] developed an expression, which is valid for spherical bubbles at $50 < Re_b < 500$. The correlations suggested by Stokes,[9] Hadamard[11]–Rybczynski,[12] and Levich[10] differ only by a constant. Based on the hydrodynamic theory of waves, Mendelson[16] proposed an expression for explicit computation of the terminal velocity of intermediate-sized bubbles in pure liquids. Fan and Tsuchiya[36] suggested an expression for the terminal velocity which is applicable for both pure and contaminated systems. Depending on the choice of coefficients, the expression by Fan and Tsuchiya[36] can be adjusted to predict a specific system. Proposed values of the coefficients are given in Table III. Other recommended values can be found in the textbook by Fan and Tsuchiya.[36] The correlation by Fan and Tsuchiya[36] includes two terms. The first term equals the correlation by Mendelson,[16] and the second term equals the correlation by Stokes,[9] Hadamard[11]–Rybczynski,[12] or Levich.[10] The coefficient applied for the second term depends on the specific system.

Tomiyama *et al.*[18] observed a dependency of the terminal velocity on the bubble aspect ratio, where the terminal velocity was pointed out to be a decreasing function of the bubble aspect ratio, E, defined as

$$E = \frac{b}{a}, \tag{3}$$

where b is the horizontal (major) bubble axis and a is the vertical (minor) bubble axis. For a spherical bubble, $a = b$, and the bubble aspect ratio in Eq. (3) will equal to unity. Tomiyama *et al.*[18] formulated a correlation to predict the terminal velocity in the ellipsoidal regime. The correlation is a function of the bubble aspect ratio, the vertical line angel, ϕ, and the distortion factor, $\gamma = 2/(1+\beta)$ (for illustration see, e.g., Tomiyama *et al.*[18]), where β is the ratio between the short and long part of the minor axis in a distorted oblate spheroidal bubble. The model is derived under the assumption of spheroidal bubbles with the distortion factor ranging from unity for ellipsoidal bubbles to a value of 2 for cap bubbles. Assuming spheroidal bubbles and the potential flow to be valid only in the vicinity of the bubble nose (Tomiyama *et al.*[18]), the model reduces to that given in Table III.

B. Drag coefficient

The drag force is an important force governing the bubble motion. Much effort has been devoted to develop accurate models for the drag coefficient.[17,26,34,46] The drag coefficient is commonly expressed in terms of dimensionless groups: Morton number [$Mo = (\rho_l - \rho_g) g \mu_l^4 / \sigma^3 \rho_l^2$], Eötvös number [$Eo = g d_b^2 (\rho_l - \rho_g)/\sigma$], bubble Reynolds number ($Re_b = \rho_l v_b d_b / \mu_l$), and Weber number ($We = \rho_l v_b^2 d_b / \sigma$). Only three of these numbers are independent, as the Eötvös number can be expressed as $Eo = Re_b^4\, Mo/We^2$.[3]

TABLE III. Correlations for the terminal velocity.

Reference	Correlation	Remarks
Stokes,[9] Hadamard[11]-Rybczynski[12]	$v_T = \frac{1}{K_b}\frac{(\rho_l - \rho_g)gd_b^2}{\mu_l}$	Spherical bubbles, immobile surfaces $Re_b < 1$, $K_b = 18, 12$ for Stokes and Hadamard–Rybczynski, respectively
Haberman and Morton[14]	$v_T = \frac{1}{18}\frac{\Delta\rho g d_b^2}{\mu_l}\left[\frac{3\mu_l + 3\mu_g}{2\mu_l + 3\mu_g}\right]$	Small bubbles
Levich (1962), referred by Ref. 36	$v_T = \frac{1}{36}\frac{(\rho_l - \rho_g)gd_b^2}{\mu_l}$	Spherical bubbles, $50 < Re_b < 500$
Mendelson[16]	$v_T = \sqrt{\frac{2\sigma}{\rho_l d_b} + \frac{gd_b}{2}}$	Intermediate to large bubbles, pure liquids
Fan and Tsuchiya[36]	$v_T = (v_{b1}^{-n} + v_{b2}^{-n})^{-1/n}$	Pure and contaminated systems
	$v_{b1} = \frac{\rho_l g d_b^2}{K_b \mu_l}$	$K_{b0} = 14.7$ (aqueous solutions)
		$K_{b0} = 10.2$ (organic solutions)
	$v_{b2} = \sqrt{\frac{2c\sigma}{\rho_l d_b} + \frac{gd_b}{2}}$	$c = 1.2$ (mono-component liquid)
		$c = 1.4$ (multi-component liquid)
	$K_b = \max(12, K_{b0}Mo^{-0.038})$	$n = 1.6$ (clean system)
		$n = 0.8$ (contaminated system)
Mendelson[45]	$v_T = \frac{v_H v_M}{\sqrt{v_H^2 + v_M^2}}$	v_H and v_M are correlations proposed by Haberman and Mendelson, respectively
Tomiyama *et al.*[18]	$v_T = \frac{\sin^{-1}\sqrt{1-E^2} - E\sqrt{1-E^2}}{1-E^2}\sqrt{\frac{8\sigma E^{4/3}}{\rho_l d} + \frac{\Delta\rho g d}{2\rho_l}\frac{E^{2/3}}{1-E^2}}$	Pure and contaminated Newtonian liquids
Baz-Rodrígues *et al.*[23]	$v_T = \frac{1}{\sqrt{(v_{T1}^2 + v_{T2}^2)^{-1}}}$	Pure liquids
	$v_{T,pot} = \frac{1}{36}\frac{\Delta\rho g d_b^2}{\mu_l}$	
	$v_{T1} = v_{T,pot}[1 + 0.73667(gd_b)^{1/2}v_{T,pot}^{-1}]^{1/2}$	
	$v_{T2} = \sqrt{\frac{3\sigma}{\rho_l d_b} + \frac{\Delta\rho g d_b}{2\rho_l}}$	

Henceforth, the bubble Reynolds number will be referred to as the Reynolds number. Table IV presents the correlations for the drag coefficient employed in the analyses of the terminal velocity in this work. All of the forces governing within each of the terminal velocity regimes, presented in Sec. II A, are involved in the proposed drag coefficients in Table IV.

Tomiyama *et al.*[17] developed a general correlation for the drag coefficient, taking into account the effects of fluid properties, gravity, bubble diameter, and contamination level characterized as clean, partly contaminated, and contaminated systems. Distilled water corresponds to a clean system, tap water corresponds to a contaminated system, and water with purity in between these categories corresponds to a partly contaminated system. It should be noted that the correlations by Ishii and Chawla[34] and Peebles and Garber[13] in Table IV are not given in their original formulations. Tomiyama *et al.*[17] rewrote the correlations by Ishii and Chawla[34] and Peebles and Garber[13] in terms of the Eötvös and Morton numbers. The drag coefficient by Peebles and Garber[13] in Table IV was rewritten by Celata *et al.*[21] in terms of the Eötvös and Weber numbers.

In a recent study by Yan *et al.*,[26] a correlation applicable for non-spherical bubbles was proposed. The existing correlations considered by Yan *et al.*[26] were found to over- or underestimate the drag coefficient when dealing with periodically fluctuating velocities. Yan *et al.*[26] proposed a new correlation for the drag coefficient, based on that by Schiller and Naumann,[47] involving the Reynolds, Weber, and Eötvös numbers for non-spherical bubbles, i.e., taking into account the bubble shape deformations. For spherical bubbles, Yan *et al.*[26] recommended the drag correlation by Tomiyama *et al.*[17] for contaminated bubbles.

TABLE IV. Correlations for the drag coefficient.

Reference	Correlation	System
Ishii and Chawla[34]	$C_D = \max\left\{\frac{24}{Re_b}\left(1+0.2Re_b^{0.75}\right), \min\left[\frac{2}{3}\sqrt{Eo}, \frac{8}{3}\right]\right\}$	
Peebles and Garber[13]	$C_D = \max\left\{\max\left(\frac{24}{Re_b}, \frac{18.7}{Re_b^{0.68}}\right), \min(0.0275EoWe^2,\ 0.82Eo^{0.25}We^{0.5})\right\}$	
Tomiyama *et al.*[17]	$C_D = \max\left\{\min\left[\frac{16}{Re_b}\left(1+0.15Re_b^{0.687}\right), \frac{48}{Re_b}\right], \frac{8}{3}\frac{Eo}{Eo+4}\right\}$	Clean
Tomiyama *et al.*[17]	$C_D = \max\left\{\min\left[\frac{24}{Re_b}(1+0.15Re_b^{0.687}), \frac{72}{Re_b}\right], \frac{8}{3}\frac{Eo}{Eo+4}\right\}$	Partly contaminated
Tomiyama *et al.*[17]	$C_D = \max\left\{\frac{24}{Re_b}(1+0.15Re_b^{0.687}), \frac{8}{3}\frac{Eo}{Eo+4}\right\}$	Contaminated
Yan *et al.*[26]	$C_D = \max\left\{\min\left(\frac{24}{Re_b}(.\,1+0.15Re_b^{0.678}), \frac{72}{Re_b}\right), \frac{24}{Re_b}(1+0.15Re_b^{0.687})\frac{Re_b^{0.55}Eo^{0.95}We^{-1.10}}{12.6}\right\}$	

The predictability of the correlation for spherical bubbles in clean water is therefore questionable.

C. Bubble aspect ratio

A common approach is to correlate the bubble aspect ratio by dimensionless numbers, such as the Eötvös, Weber, and Tadaki numbers. Table V presents correlations for the bubble aspect ratio in terms of the Eötvös and Weber numbers. Tomiyama *et al.*[48] observed a strong correlation between the bubble aspect ratio and the Weber number. Formulations on the basis of the Eötvös number have been stated to be inaccurate due to the dependency of the detachment condition, i.e., the initial bubble deformations. Close to spherical bubbles deform to a smaller extent and are less affected by the detachment condition. Okawa *et al.*[19] argued that formulations for the bubble aspect ratio in terms of the Eötvös number should be restricted to smaller bubbles. For a close to spherical bubble, rising under the assumption of inviscid flow around the bubble surface, Moore[49] derived the following correlation:

$$We = 4\chi^{-4/3}\frac{(\chi^3+\chi-2)\left[\chi^2\sin^{-1}\chi-\chi\sqrt{\chi^2-1}\right]^2}{(\chi^2-1)^{-3}}, \quad (4)$$

where χ is the reciprocal of the bubble aspect ratio.

For low-viscosity liquids, $Mo < 2.5\times10^{-4}$, Tadaki and Maeda[51] proposed the following correlations for the bubble aspect ratio based on a dimensionless group, later referred to as the Tadaki number, $Ta = ReMo^{0.23}$:[28]

$$\frac{d_b}{b} = \begin{cases} 1, & Ta < 2, \quad (5a)\\ 1.14Ta^{-0.176}, & 2 < Ta < 6, \quad (5b)\\ 1.36Ta^{-0.28}, & 6 < Ta < 16.5, \quad (5c)\\ 0.62, & 16.5 < Ta, \quad (5d)\end{cases}$$

TABLE V. Correlations for the bubble aspect ratio based on the Eötvös and Weber numbers.

Reference	Correlation	Note
Wellek *et al.*[50]	$E = \frac{1}{1+0.163Eo^{0.757}}$	Non-oscillating drops, contaminated liquid
Okawa *et al.*[19]	$E = \frac{1}{1+0.163Eo^{1.3}}$	Modification of Wellek
Sanada *et al.*[22]	$E = \frac{1}{1+6.5Eo^{1.925}}$	Fitted to experimental data
Moore[49]	$E = \frac{1}{1+\frac{9}{64}We}$	Approximation of Eq. (4)
Taylor and Acrivos	$E = \frac{1}{1+\frac{5}{32}We}$	Originally developed for creeping flow
Wellek *et al.*[50]	$E = \frac{1}{1+0.091We^{0.95}}$	Non-oscillating drops, fairly contaminated liquid

where $d_b/b = E^{1/3}$ for ellipsoidal bubbles.

Vakhrushev and Efremov[52] modified the correlation by Tadaki and Maeda:[51]

$$E = \begin{cases} 1, & \mathrm{Ta} < \mathrm{Ta}_1, \quad (6a) \\ c_1 + c_2 \tanh\left[c_3(c_4 - \log_{10})\mathrm{Ta}\right]\}^2, & \mathrm{Ta}_1 < \mathrm{Ta} < \mathrm{Ta}_2, \quad (6b) \\ c_5, & \mathrm{Ta}_2 < \mathrm{Ta}, \quad (6c) \end{cases}$$

where, for pure water, Fan and Tsuchiya[36] suggested the following parameter values: $c_1 = 0.77$, $c_2 = 0.24$, $c_3 = 1.19$, $c_4 = 0.40$, $c_5 = 0.30$, $\mathrm{Ta}_1 = 0.3$, and $\mathrm{Ta}_2 = 20$.

III. EXPERIMENTAL SETUP

Single bubble experiments are carried out in a vertical column with dimensions $200 \times 4 \times 4$ cm^3, as illustrated in Fig. 1. Column walls made of plexiglass allow for image recording of the single bubble as it rises through the column. An individual single bubble is generated through a glass needle using a syringe pump (KdScientific Legato200). By varying the nozzle size, the initial size of the bubble can be varied. To capture the evolution of a bubble during its rise through the column, a high-speed camera (Photron FASTCAM MINI AX100) with a lens (Navitar 6.5× zoom with 12 mm fine focus, and a 1× F-mount adapter) is installed on a linear unit drive (ISEL LES5, Controller MC 1–20) parallel to the column. Images are recorded at a frame rate of 1000 fps and shutter speed in the range of 1/12 000–1/18 000 s. Henceforth, this camera is referred to as *camera I*. Depending on the bubble size injected, the images capture a physical space between 20×20 and 28×28 mm^2 of the column (image resolution is 1024×1024 px^2). Images recorded by camera I are locally stored in the memory of the camera during the bubble rise event and thus not available for analysis in the computer software during this time. To allow for real-time analyses of images, a second high-speed camera (AOS PROMON U750) is installed on the linear unit drive, similar to camera I. This high-speed camera, which is referred to as *camera II*, transfers real-time recorded images to the computer for analysis of the bubble position, which in turn is used to adjust the velocity of the linear unit drive. Camera II is operated at a frame rate of 25 fps and exposure time 300 ms. A light-emitting diode (LED) (MultiLed QT+, GSVitec, with luminous flux white, 12 000 lumen, and power 150 W) is located opposing the cameras, and a diffusion paper attached to the associated wall ensures homogeneous light distribution and elimination of reflections from the bubble surface or the column walls. The LED diode is connected to a multiLED G8 controller (GSVitec).

Deionized water at room temperature of 23° C is used as the continuous phase. The inlet water is purified by a purification system (pretreatment (Progard) and Millipore RiOS150), removing 95%–99% of the ions and 99% of dissolved organic substances, microorganisms, and particles. The liquid phase oxygen concentration is measured using dissolved oxygen probes (METTLER TOLEDO InPro6860i). Three dissolved oxygen probes are installed on the column. The probes are used to ensure that the water is saturated with air, i.e., that there is a net-zero mass transfer between the bubble and the continuous phase. The system components, that is, the syringe pump, the linear unit drive, and the two high-speed cameras, are controlled through the software National Instruments LabVIEW. An outline of the working principles of the system control is given in Sec. IV. The description of the system control includes the image processing by camera II and the system control of the linear unit drive. The analysis of the images obtained by camera I, used for evaluation of the bubble properties, is outlined in Sec. V.

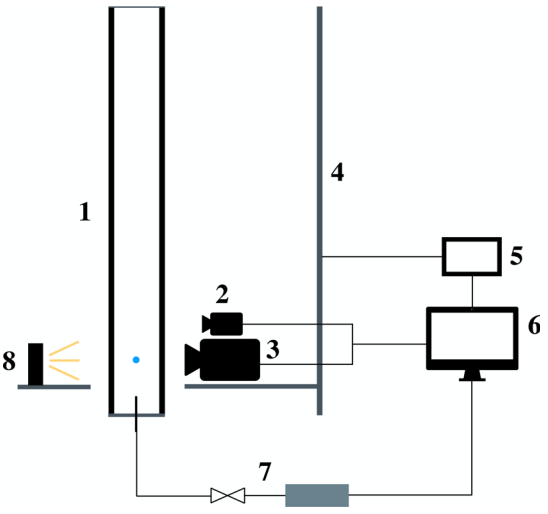

FIG. 1. The experimental facility is composed of (1) liquid column, (2) camera II, (3) camera I, (4) linear unit drive, (5) controller, (6) computer, (7) syringe pump, (8) LED panel.

IV. AUTOMATION OF THE EXPERIMENTAL SETUP

A. Image analysis to determine the linear unit drive velocity—Camera II

To adapt the linear unit drive to the velocity of a bubble rising in the column, images from camera II are continuously processed in LabVIEW. An original image recorded by camera II is shown in Fig. 2. The bars present on the LHS of the column in Fig. 2 are used as a reference of length to estimate the position and velocity of the linear unit drive. The bars on the RHS are used by camera I in the image processing and analysis to determine the bubble properties, as described in Sec. V. Operated at a frame rate of 25 fps, camera II is not able to

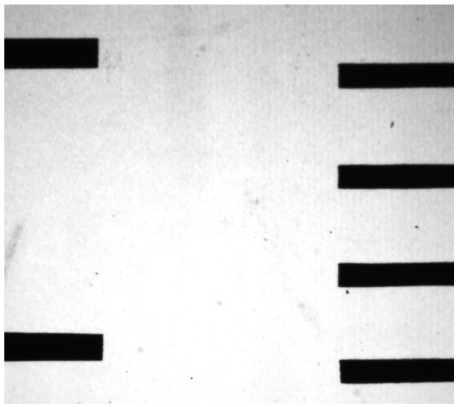

FIG. 2. Original image recorded by camera II.

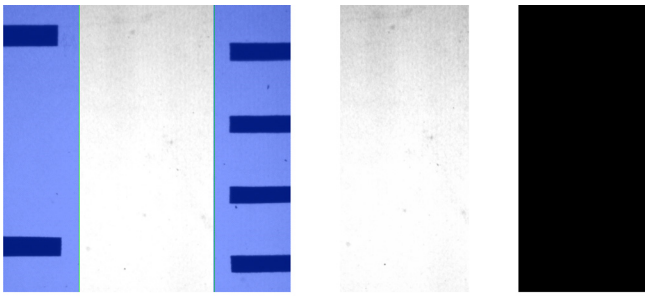

FIG. 3. (a) Original image including the selected region to be discarded, (b) cropped image, and (c) binarized image used in the bubble data processing.

process bars with a spatial distance less than 18 mm. Hence, two sets of bars are employed to meet the constraints by camera I and II.

Two regions of interest (ROI) are extracted from the image in Fig. 2. The blue/darker areas in Figs. 3(a) and 4(a) are the areas to be neglected from the original image in Fig. 2. Figures 3(b) and 4(b) show the resulting cropped ROIs. Prior to the binarization of the images in Figs. 3(b) and 4(b), threshold values are pre-selected. The threshold values are chosen to eliminate pixels not related to the bubble or the bars. The final binarized images of the two ROIs are shown in Figs. 3(c) and 4(c), where Fig. 3(c) captures the ascending bubble and Fig. 4(c) includes the bars, which are employed to calculate the velocity and position of the bubble and the linear unit drive.

B. System control—Bubble tracking and linear unit drive velocity

To adapt to the transient motion of an ascending bubble, the velocity of the linear unit drive is continuously updated. This is done by estimating the instantaneous bubble velocity from the images obtained by camera II. Henceforth, time (t), all velocities (v), and position (y, x) are given in units ms, cm/s, and px, respectively. The bubble velocity relative to camera II, $v_{\mathrm{rel,b}}$, is obtained by dividing the change in the bubble position between two consecutive images, Δx_{b}, by the time between the two recorded images, Δt:

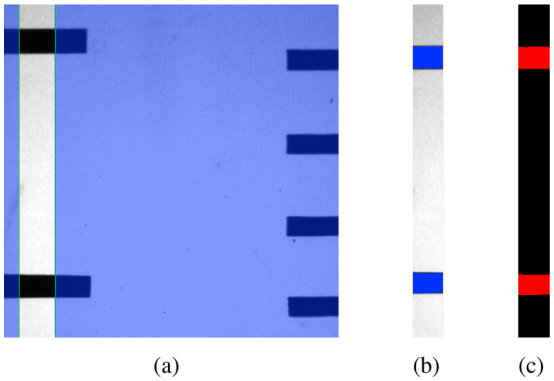

FIG. 4. (a) Original image including the selected region to be discarded, (b) cropped image, and (c) binarized image of the bars used in the linear unit drive velocity control.

$$v_{\mathrm{rel,b}} = \zeta \frac{\Delta x_{\mathrm{b}}}{\Delta \mathrm{t}}, \tag{7}$$

where ζ denotes the scaling factor from px to mm.

The absolute bubble velocity, v_{b}, is calculated as the sum of the relative bubble velocity and the velocity of the linear unit drive, v_{lud}:

$$v_{\mathrm{b}} = v_{\mathrm{rel,b}} + v_{\mathrm{lud}}. \tag{8}$$

The position of the linear unit drive, $\mathrm{x_l}$, and the scaling factor is obtained by using the bars fixed on the column wall, as shown in Fig. 4(c). By performing a linear regression, the position of the bars, y_{bar}, is obtained for each image:

$$y_{\mathrm{bar}} = \zeta m_{\mathrm{bar}} + \mathrm{x_l}, \tag{9}$$

where m_{bar} is the number of bars present in the image. ζ and $\mathrm{x_l}$ are obtained as the coefficients from the linear regression.

The velocity of the linear unit drive is calculated as the ratio between the change in the position of the linear unit drive and the time between two consecutive frames:

$$v_{\mathrm{lud}} = \zeta \frac{\Delta x_{\mathrm{l}}}{\Delta \mathrm{t}}. \tag{10}$$

There is a time delay in the command signal sent from the computer software to the linear unit drive, and the time at which the command is actuated by the linear unit drive. To compensate for the time delay, the change in the bubble velocity is anticipated. The compensating velocity, v_{++}, is obtained by linear regression where a fraction of the previous bubble velocity is used. The time delay is further elaborated in Sec. IV C. Due to the limited range of view of camera II, a bubble easily moves out of the ROI. In an attempt to tune the bubble toward the center of the image, a second compensating velocity, denoted centering velocity, is introduced. The centering velocity, v_{c}, is found by estimating the required change in the linear unit drive velocity in order to tune the bubble toward the center of the image. The final velocity sent to the linear unit drive, v_{sp}, is calculated by Eq. (11),

$$v_{\mathrm{sp}} = v_{\mathrm{b}} + k_1 v_{\mathrm{c}} + k_2 \Delta v_{++}, \tag{11}$$

where k_1 and k_2 are controller constants. k_1 affects the velocity at which the bubble will move toward the center of the image. k_2 affects the compensation of the delay in the linear unit drive.

C. Processed data

The presence of a delay in the experimental setup results in a delay in the initial movement of the linear unit drive. In addition, the delay is reflected in a late adaption of the linear unit drive to a new set velocity. The combined effects of the dynamic bubble ascent and the delay in the linear unit drive result in an intricate system. The system acquires the ability to rapidly adjust to changes in the bubble velocity. During a bubble rise event, a data set is generated through camera II. The data set contains preliminary information about the bubble position, velocity, and size, in addition to the velocity of the linear unit drive. The preliminary information can be used to assess the correspondence between the velocities v_{b}, v_{lud}, and v_{sp}. In addition, the preliminary information can be employed to study the effect of adjusting the controller parameters, k_1 and k_2.

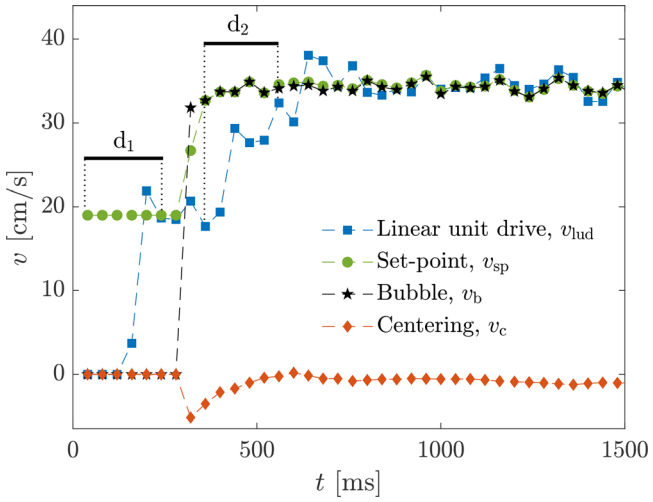

FIG. 5. Example of a delay in the actuation time of the linear unit drive, comparing the linear unit drive velocity, v_{lud}, the set velocity, v_{sp}, the centering velocity, v_c, and the velocity of the bubble, v_b.

Due to the delayed initial movement, the linear unit drive is activated prior to the injection of a bubble. In the example shown in Fig. 5, the linear unit drive is given an initial set velocity of $v_{sp} = 18$ cm/s. Note that the initial set velocity must be chosen depending on the initial bubble velocity. The velocity of the linear unit drive, v_{lud}, reaches the set-point velocity after six time-steps, noted by d_1 in Fig. 5. When the injected bubble reaches the ROI, the bubble velocity, v_b, is estimated, and a new set-point velocity is calculated. The set-point and bubble velocity are seen to correspond well in Fig. 5. The linear unit drive adapts to the new set-point velocity after six time-steps, noted by d_2 in Fig. 5. As the velocity of the linear unit drive increases above the bubble velocity, the centering velocity, v_c, is correcting by a negative value. To assess the average time delay in the adaption of the linear unit drive to the set-point velocity, 30 bubble rise events were evaluated. The average time delay is 250 ms. There is a significant correspondence between the bubble and set-point velocity, seen by the approximately overlapping velocities in Fig. 5. The delay in the actuation time of the linear unit drive is concluded to be mechanical.

V. IMAGE ANALYSIS OF BUBBLE PROPERTIES—CAMERA I

An in-house image processing algorithm in MATLAB (2020a) is used to determine the bubble properties from the images recorded by camera I. Prior to the computation of the bubble properties, the original images are processed. The image processing consists of the following steps: (1) image cropping, (2) subtraction of a background image, (3) binarization, (4) image filling, (5) image imcomplement, and (6) parameter extraction. The resulting images from the processing steps are shown in Fig. 6.

Image processing: Cropping (step 1)

The original grayscale image in Fig. 7(a) shows an ascending bubble, including the bars employed to determine the bubble velocity and position. A grayscale image contains pixels with values in the range of 0 to 255. An 8-bit representation is used, which means that the image is stored with 8 bits per sampled pixel.[53] In the first step of the image processing, the original image in Fig. 7(a) is cropped into two ROI. One ROI includes the bubble, shown in Fig. 7(b), and the second ROI includes the bars, shown in Fig. 7(c).

Image processing: Contrast enhancement (step 2)

All the elements that are not related to the bubble are removed. This is done by subtracting image (a) in Fig. 6 by a background image. The background image is calculated as the average of the bubble rise path. Figure 6(b) shows the result when the background image is subtracted by the current image. The complement of image (b) in Fig. 6 is computed using the MATLAB built-in function *imcomplement*. When complementing a grayscale image, the pixels are subtracted from the maximum pixel value. This results in the dark areas becoming brighter, and vice versa. The resulting complemented image is shown in Fig. 6(c).

Image processing: Binarization (step 3)

In a binary image, the pixels can take the value of 0 (black) or 1 (white). Prior to the binarization of a grayscale image, a threshold, T, is calculated. All the pixels with a value above the threshold are replaced by the value of 1, and all others are set to 0. In the present work, a threshold is calculated for each of the recorded images. For a bubble rise event containing 7000 images, 7000 corresponding threshold values are obtained. The thresholds are obtained by means of *graythresh*, a built-in MATLAB-function. *Graythresh* uses Otsu's method,[54] where the values are chosen to minimize the intraclass variance of black and white pixels. Conversion to a binary image is executed using the MATLAB built-in function *imbinarize*. The binarized image is shown in Fig. 6(d).

Determining a suitable threshold value is of crucial importance, as it determines the bubble edge. In Fig. 8(a), an original grayscale image of an ellipsoidal bubble is shown. To illustrate the transition from dark to brighter pixels on the bubble edge, an enlarged area of the ellipsoidal bubble is shown in Fig. 8(b). When an image is binarized, the threshold value will determine if a pixel on the bubble edge is associated with the bubble or the background. Figure 8(c) shows a bubble where the original (pink) and binarized (green) images have been joined, i.e., the binarized image is placed on top of the original. An enlarged part of the joined image is shown in Fig. 8(d). Comparing Figs. 8(b) and 8(d), the discarded pixels (pink) correspond to pixels which could be associated with both the bubble and the background. Assessing the discarded pixels on the bubble edge in Fig. 8(d), the major and minor axes lengths are well represented. The choice of threshold is further elaborated in Sec. V B.

Image processing: Filling (step 4)

Due to the illumination of the vertical column, a bright spot is present at the center of the bubble in Fig. 6(d). The spot is eliminated by setting all the relevant values to 0, using the MATLAB built-in function *bwareaopen*. *bwareaopen* removes all the connected objects, which contain less than a specific number of pixels. The resulting filled bubble is shown in Fig. 6(e).

Image processing: Imcomplement (step 5)

The bubble parameters are extracted by using the MATLAB built-in function *regionprops*. *regionprops* calculates the properties of an object by regarding connected pixels of value 1. The bubble in Fig. 6(e) is defined by zero-valued pixels. Thus, the image needs to be complemented prior to the extraction of the bubble parameters. Black and white areas in the binary image are switched by using the function *imcomplement*, as in step 2 of the image processing. The resulting image of a white bubble with a black background is shown in Fig. 6(f).

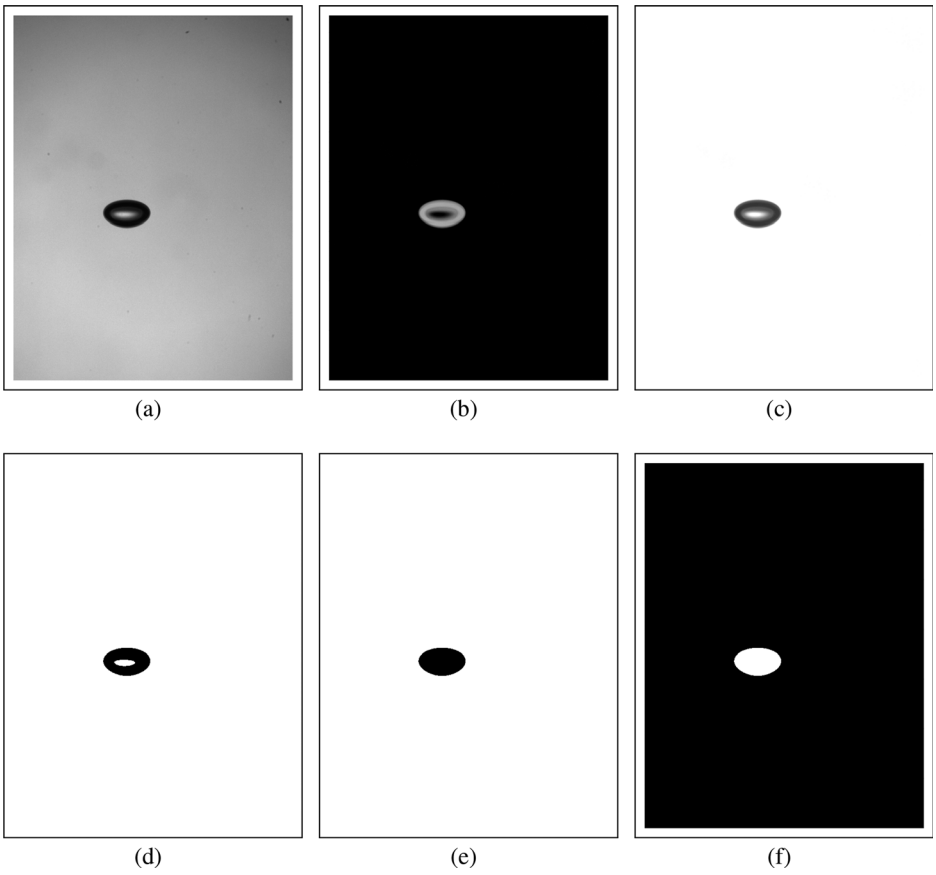

FIG. 6. Example of resulting images after handled by the image processing algorithm in MATLAB (2020a). Images (a)–(f) are obtained in image processing steps 1–6, respectively.

Image processing: Parameter extraction (step 6)

The bubble area (number of pixels defining the bubble), centroids (x,y-position), and major and minor axes lengths are calculated by using the function *regionprops*. For larger bubbles where the shape largely deviates from a spherical or ellipsoidal shape, determining the bubble diameter, aspect ratio, and the terminal velocity based on 2D images is challenging. This is particularly demanding when analyzing bubbles that exhibit significant bubble shape oscillations, and where the bubble rise paths are observed to be zigzag or helical. In the studies of Okawa *et al.*,[19] Celata *et al.*,[20] Liu *et al.*,[24] and Yan *et al.*,[26] bubble data obtained by image acquisition from one- and two sides of a bubble were compared. The bubble data generated from one side of the bubble were found to sufficiently approximate the actual process within an error of ±10%. The bubbles observed by Okawa *et al.*,[19] Celata *et al.*,[20] Liu *et al.*,[24] and Yan *et al.*[26] were equal or larger in size than those analyzed in the present work. Hence, evaluating the bubble properties based on images recorded from one direction is considered to be sufficient for the present experimental work.

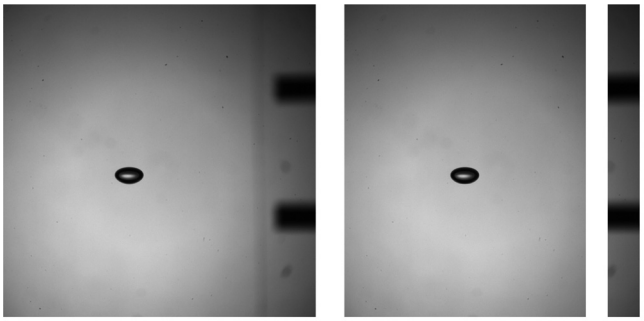

FIG. 7. (a) original image of an ellipsoidal air bubble in water, as recorded by camera I, (b) cropped ROI including the bubble, (c) cropped ROI including the bars.

A. Analysis of bubble properties: Bubble velocity

The bubble velocity is calculated by Eqs. (12)–(16),

$$v_{b,k} = \frac{\sqrt{(\Delta y_{bar} - \Delta y_b)^2 + (\Delta x_{bar} - \Delta x_b)^2}}{\Delta t}, \tag{12}$$

$$\Delta y_b = y_{b,k+1} - y_{b,k}, \tag{13}$$

$$\Delta x_b = x_{b,k+1} - x_{b,k}, \tag{14}$$

$$\Delta y_{bar} = y_{bar,k+1} - y_{bar,k}, \tag{15}$$

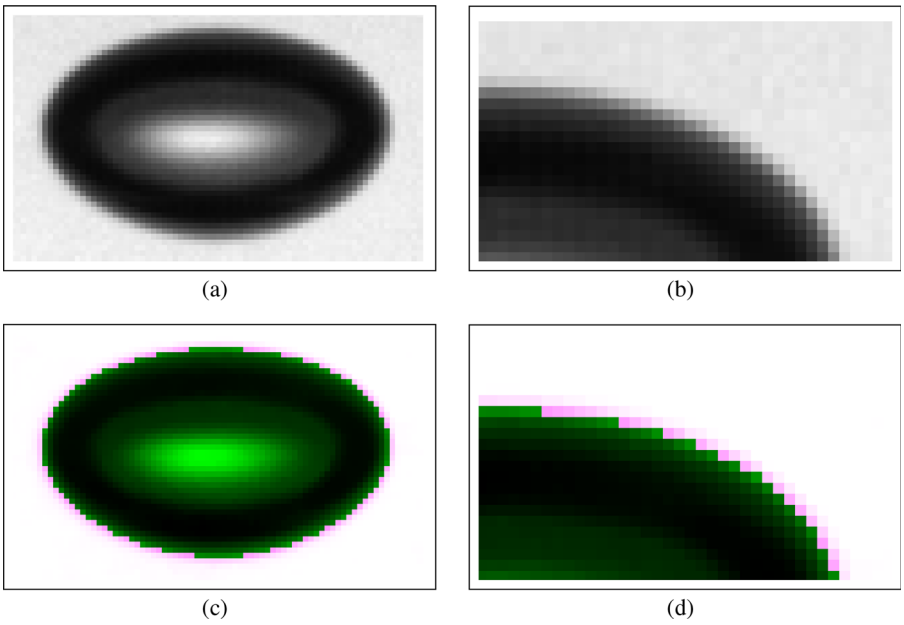

FIG. 8. (a) original image of an ellipsoidal bubble, (b) enlarged region of the original image, (c) joined original (pink) and binarized (green) image, (d) enlarged region of the joined original and binarized image.

$$\Delta x_{\mathrm{bar}} = x_{\mathrm{bar,k+1}} - x_{\mathrm{bar,k}}, \tag{16}$$

where Δy_{bar}, Δy_{b} and Δx_{bar}, Δx_{b} are the changes in the bar and bubble epicenter between two consecutive images in y- and x-direction, respectively. $\Delta t = t_{\mathrm{k+1}} - t_{\mathrm{k}}$ is the time step.

Figure 9 illustrates the change in position of the bars and the bubble between two consecutive images. Due to the mechanical delay in the linear unit drive, the adaption to a new set velocity may be delayed. This can result in the bubble moving away from the center or out of the image. Thus, the change in position of the bubble and bars in Fig. 9 depends both on the velocity of the bubble and the linear unit drive.

The procedure for calculating the terminal velocity is illustrated in Fig. 10. The term bubble velocity, denoted v_{b}, is used here for the instantaneous bubble velocity, whereas the term terminal velocity, denoted v_{T}, describes the time averaged bubble velocity in which only the vertical component of the velocity vector is considered. The presented experimental results on the terminal velocity are average values based on multiple bubble rise events. Typically, $N = 10$–20 bubble rise events are considered when calculating the average terminal velocity. The number of necessary bubble rise events is statistically evaluated in Sec. VII E. As a needle may produce bubbles of slightly different size, the bubbles are grouped according to their initial size. The bubble velocity in Fig. 10 is a mean value based on 22 independent bubble rise events, with a mean bubble diameter $d_{\mathrm{b}} = 1.15$ mm. Hence, the z-axis in Fig. 10 represents an approximated position for the mean bubble velocity. Instantly after the bubble detaches from the needle, it accelerates and an increase in the bubble velocity is observed. In this work, it is the terminal velocity that is of interest, and the first part of the bubble velocity profile in Fig. 10 is therefore neglected. When a force balance is obtained, the bubble reaches a terminal velocity, estimated by linear regression over the inspected time interval. Reaching the top of the column, the bubble moves out of the image. Hence, the bubble velocity data from the upper part of the column are neglected. The inspected time interval is manually determined for each of the bubble rise events.

B. Analysis of bubble properties: Bubble diameter

The volume equivalent bubble diameter, d_{b}, is calculated from the projected area and the minor and major axes of an ellipsoid, under the assumption of an oblate spheroid:

$$d_{\mathrm{b}} = \sqrt[3]{(2b)^2 \times (2a)}, \tag{17}$$

where $A = 2a$ and $B = 2b$ are the minor (vertical) axis and major (horizontal) axis, respectively. For a spherical bubble, the minor axis and major axis equals, and Eq. (17) reduces to that of a sphere.

A sensitivity analysis was performed to assess the influence of the threshold value on the calculated bubble diameter. In the sensitivity analysis, seven threshold values were evaluated. The influence of the threshold on the bubble diameter is illustrated in Fig. 11. Six values, $T \in [0.55, 0.90]$, were held constant for all time instants during the image processing. The relative difference in the calculated average bubble diameter when using $T = 0.55$ and $T = 0.9$ is 6 %. In addition, a threshold, denoted local threshold, was calculated for all time instants. A local threshold will capture potential changes in the illumination along the vertical column. The variation in the calculated local threshold as a function of time is shown in Fig. 11.

The original and binarized images for the various thresholds were joined, as illustrated in Fig. 8. Assessing the joined images revealed misrepresented pixels on the bubble edge. The bubble diameter was underestimated for $T = 0.55$ and overestimated for $T = 0.90$. When using $T = 0.90$, all the pixels associated with the bubble were

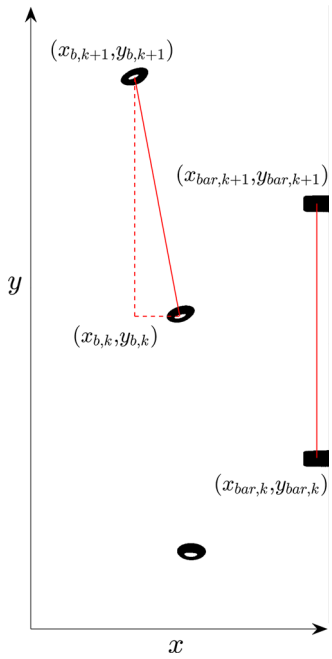

FIG. 9. Change in the vertical and horizontal position of the bars and the bubble between image k and $k+1$.

included. However, $T = 0.90$ resulted in the inclusion of pixels associated with shadows on the bubble edge due to curvature. Approximately the same values of the characteristic lengths of the bubble were obtained when using a local threshold and $T = 0.90$. However, pixels associated with shadows on the bubble edge were not included when using a locally calculated threshold. Based on the visual

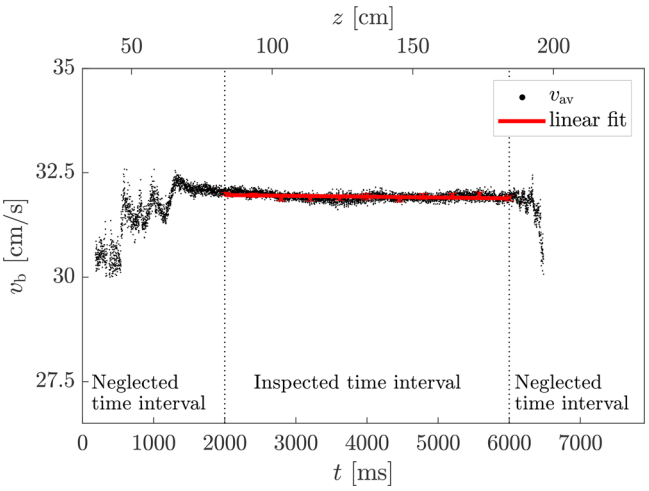

FIG. 10. Procedure for calculating the terminal velocity. The bubble velocity in the specific example is based on 22 bubble rise events, with a mean bubble diameter of $d_b = 1.15$ mm.

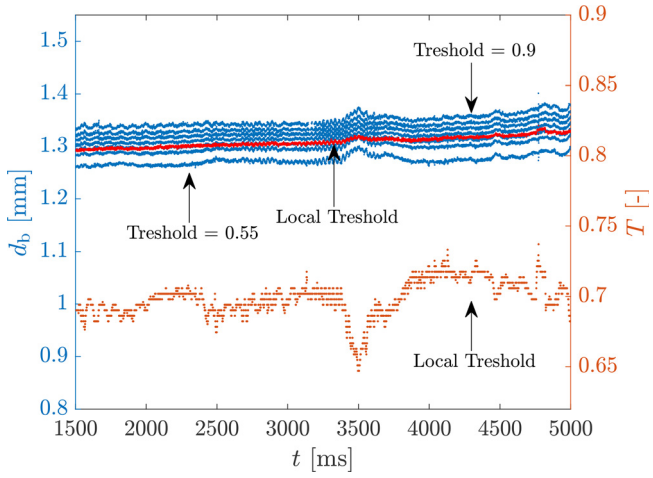

FIG. 11. Calculated volume equivalent bubble diameter as function of time, using $T \in [0.55, 0.90]$ and a local threshold.

inspection of the joined images, a local threshold gives the most accurate representation of the bubble edge. The uncertainties in the major axis and minor axis are assumed to be ± 1 px based on the visual assessment of the joined images.

C. Threshold bars

The images containing bars were given a separate threshold value in the binarization. Due to the bars being located at a focal plane out of focus, as shown in Fig. 7(c), an accurate representation of the bars' position is challenging. Calculating the threshold by use of the MATLAB built-in function *graytresh* gave an inaccurate representation of the bars. The *graytresh* function included regions that were not associated with the bars. When measuring the displacement between two consecutive images, the center position of the bars is being measured. The influence of the bars, being out of focus, on the measured center position was quantitatively and visually evaluated. If the gray tones were equally spaced above and below the bars, the measured center position was unaffected. This requirement was met by determining an appropriate threshold value. The value was chosen by assessing the original and binarized images when using various threshold values. Three independent experimental events were evaluated using seven different threshold values. Figure 12 illustrates the effect for one of the experimental events. Lower values, $T \in [0.65, 0.80]$, resulted in scattering bubble velocity data. The original and binarized images were joined when using $T \in [0.65, 0.80]$, which revealed the inclusion of darker areas not associated with the bars. Using higher values, $T \in [0.85, 0.95]$, parts of the gray-scale areas associated with the bars were discarded. The edges of the bars were defined and clear when using $T \in [0.85, 0.95]$. In the algorithm, a bar is evaluated when present within a certain vertical range. The vertical limits are chosen to ensure that at least one of the present bars is being evaluated. The presence of at least two bars in the image assures that a bar is always within the vertical range.

The calculated bubble velocity was compared at four heights along the vertical column, using $T = [0.85, 0.9, 0.95]$. The largest

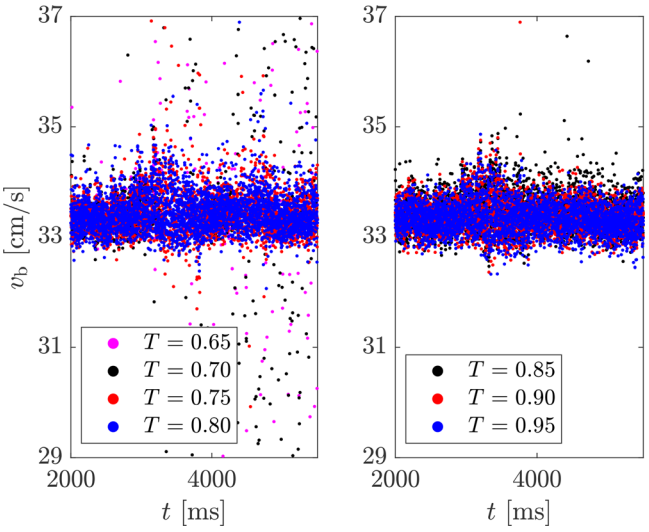

FIG. 12. Influence of varying threshold values used in the image processing of the bars on the calculated bubble velocity.

relative difference in the bubble velocity between the heights was 0.3% for $T = 0.85$, 0.3% for $T = 0.9$, and 0.2% for $T = 0.95$. In the present work, the bubble velocity range is $v_b \in [12, 39]$ cm/s. While $T \geq 0.85$, the choice of threshold value has negligible effect on the calculated bubble velocity.

VI. STATISTICAL DATA TREATMENT

The experimental data may be subject to several sources of error associated with the experimental setup and image analysis. Random errors are reflected in the standard deviation and the confidence interval of the experimental data.

When measurements can be repeated several times, and the associated uncertainties are known to be random, the uncertainty in a quantity can be estimated by examining the spread in the calculated data. In the present work, the calculated quantities are average values of multiple experimental events. The mean, $\bar{x}$, and the sample standard deviation, S, can be calculated by the general formulas given in Appendix B.[55]

Calculating the bubble velocity and diameter involves two steps. First, the quantities that are possible to measure, e.g., bubble position and axes lengths, are measured. Second, the quantities of interest, e.g., the terminal velocity and bubble diameter, are calculated based on the measurements. The uncertainty in the calculated quantity is a function of the uncertainties of the directly measured quantities. The uncertainties in the directly measured quantities propagate through the calculation to produce the uncertainty in the final calculated quantity (Taylor[55]). For a parameter Y, as function of n measured independent variables $(y_1, \ldots, y_n)$ whose uncertainties $\delta y_1, \ldots, \delta y_n$ are small, that is, $Y = f(y_1, y_2, \ldots, y_n)$, the uncertainty can be found by the multivariate propagation of error formula in Eq. (18) (Ref. 56),

$$(\delta Y)^2 = \left(\frac{\partial Y}{\partial y_1}\delta y_1\right)^2 + \left(\frac{\partial Y}{\partial y_2}\delta y_2\right)^2 + \cdots + \left(\frac{\partial Y}{\partial y_n}\delta y_n\right)^2, \quad (18)$$

where the uncertainty of each variable is represented by $\delta y_1, \ldots, \delta y_n$. Note that the variables in Eq. (18) are assumed to be independent, i.e., the covariances between the variables are zero. The uncertainty obtained by Eq. (18), δY, is the absolute uncertainty of Y. The relative uncertainty can be found by dividing δY by the value of Y.

If the uncertainty can be calculated by both the propagation of errors and by regarding the standard deviation of the mean from multiple experimental runs, both methods should be applied and compared (Taylor[55]). The two methods should give approximately the same values:

Terminal velocity

The instantaneous bubble velocity can be formulated as

$$v_{b,k} = \frac{s}{\Delta t}\sqrt{\left[(P_{ybar,k+1} - P_{ybar,k}) - (P_{yb,k+1} - P_{yb,k})\right]^2 + \left[(P_{xbar,k+1} - P_{xbar,k}) - (P_{xb,k+1} - P_{xb,k})\right]^2}, \quad (19)$$

where $s = h_{cal,m}/h_{cal,px}$ denotes the scaling factor from unit pixels to unit length, $h_{cal,m}$ and $h_{cal,px}$ are the widths in units of length and pixels, respectively, Δt the time step between two consecutive images, and $P_{ybar,k+1}$, $P_{ybar,k}$, $P_{yb,k+1}$, and $P_{yb,k}$ refer to the position in y-direction of the evaluated bar and bubble at image number $k+1$ and k. $P_{xbar,k+1}$, $P_{xbar,k}$, $P_{xb,k+1}$, and $P_{xb,k}$ refer to the position in x-direction of the evaluated bar and bubble at image number $k+1$ and k. P is given in unit of pixels.

The absolute random uncertainty in the terminal bubble velocity, $\delta v_{T,r}$, can be calculated from the propagation of error in Eq. (18) and the instantaneous bubble velocity in Eq. (19), where the latter equation is reduced to only contain the vertical component y. The relative uncertainty can be found by dividing Eq. (20) by the terminal velocity. The partial derivatives in Eq. (20) are derived in Appendix C.

$$\delta v_{T,r} = \left[\left(\frac{\partial v_b}{\partial P_{ybar,k+1}}\delta P_{ybar,k+1}\right)^2 + \left(\frac{\partial v_b}{\partial P_{ybar,k}}\delta P_{ybar,k}\right)^2 + \left(\frac{\partial v_{yb}}{\partial P_{yb,k+1}}\delta P_{yb,k+1}\right)^2 \left(\frac{\partial v_b}{\partial P_{yb,k}}\delta P_{yb,k}\right)^2 + \left(\frac{\partial v_b}{\partial \Delta t}\delta \Delta t\right)^2\right]^{1/2}, \quad (20)$$

where $\delta P_{ybar,k+1}$ and $\delta P_{ybar,k}$ are the uncertainties in the bar position in y-direction at image number $k+1$ and k, $\delta P_{yb,k+1}$ and $\delta P_{yb,k}$ the uncertainties in the bubble position in y-direction at image number $k+1$ and k, and $\delta \Delta t$ the uncertainty in the time step between two consecutive images.

The vertical displacement of the bubble and the bars in Eq. (20) are considered over the time interval over which the terminal velocity

is calculated. Thus, the displacement is considered over multiple images.

Bubble diameter

The absolute random uncertainty in the bubble diameter, $\delta d_{b,r}$, is calculated by Eq. (21). The relative random uncertainty can be obtained by dividing Eq. (21) by the bubble diameter. The partial derivatives in Eq. (21) are derived in Appendix C.

$$\delta d_{b,r} = \sqrt{\left(\frac{\partial d_b}{\partial A}\delta A\right)^2 + \left(\frac{\partial d_b}{\partial B}\delta B\right)^2}, \tag{21}$$

where δA and δB denote the uncertainties in the minor and major axes lengths, respectively.

Note that the minor and major axes lengths are taken to be mean values over the corresponding time interval over which the terminal velocity is calculated.

A. Uncertainty in the scaling factor

A rectangular glass pin marked with a horizontal line is used to obtain the scaling factor from unit pixels (px) to unit length (mm). The length of a pixel is calculated from the number of pixels and the width in unit length of the horizontal line on the glass pin. The uncertainty in the px-to-mm scaling factor arises from the uncertainty in the measurement of the calibration pin in unit pixels, $\delta h_{cal,px}$, and the uncertainty in the measurement in unit length, $\delta h_{cal,m}$. It is assumed an uncertainty of ± 0.5 px on each side of the rectangular pin, i.e., $\delta h_{cal,px} = \pm 1$ px. Digital equipment (Mitutoyo digital ABS Caliper CoolantProof IP67) was used to measure the width of the calibration pin in unit length. The uncertainty in the digital equipment is reported by the producer to be $\delta h_{cal,m} = \pm 0.02$ mm. The depth at which the calibration pin is measured corresponds to that at which the bubbles are produced.

The uncertainty in the px-to-mm scaling factor can be calculated from the propagation of error formula in Eq. (18).[55] The contribution from the uncertainty in the px-to-mm scaling factor to the absolute random uncertainty in the terminal velocity, $\delta v_{T,c}$, and the bubble diameter, $\delta d_{b,c}$, are given by Eqs. (22) and (23) as follows:

$$\delta v_{T,c} = \sqrt{\left(\frac{\partial v_b}{\partial h_{cal,m}}\delta h_{cal,m}\right)^2 + \left(\frac{\partial v_b}{\partial h_{cal,px}}\delta h_{cal,px}\right)^2}, \tag{22}$$

$$\delta d_{b,c} = \sqrt{\left(\frac{\partial d_b}{\partial h_{cal,m}}\delta h_{cal,m}\right)^2 + \left(\frac{d_b}{\partial h_{cal,px}}\delta h_{cal,px}\right)^2}. \tag{23}$$

The total random uncertainties in the terminal velocity and the bubble diameter are given by Eqs. (24) and (25):

$$\delta v_{T,tot} = \sqrt{\delta v_{T,r}{}^2 + \delta v_{T,c}{}^2}, \tag{24}$$

$$\delta d_{b,tot} = \sqrt{\delta d_{b,r}{}^2 + \delta d_{b,c}{}^2}. \tag{25}$$

It should be noted that the uncertainty in the px-to-mm scaling factor is explicitly accounted for when employing the propagation of error formula in Eq. (18), which is not the case when the uncertainty is calculated from the repeat of measurements in Eq. (33).

TABLE VI. Values used to calculate the uncertainties in the bubble velocity and diameter.

Parameter	Unit	Value
ΔP_{ybar}	px	9–18
ΔP_{yb}	px	0.3–0.6
Δt	s	10^{-3}
$h_{cal,m}$	mm	3.77
$h_{cal,px}$	px	154–194
A	px	38–61
B	px	39–111
δP_{bar}	px	± 1
δP_b	px	± 1
$\delta h_{cal,m}$	mm	± 0.02
$\delta h_{cal,px}$	px	± 1
$\delta \Delta t$	s	$\pm 10^{-6}$
δA	px	± 1
δB	px	± 1

The values applied to calculate the uncertainties in the terminal velocity and the bubble diameter are given in Table VI.

VII. RESULTS AND DISCUSSION

A. Bubble rise velocity

Instantly after a bubble detaches from the needle, the bubble accelerates until buoyancy, gravity, and drag forces are balanced, and the terminal velocity is reached. In Fig. 13, the bubble velocity as a function of time is plotted for bubbles of volume equivalent diameter $d_b = 1.15, 1.28,$ and 1.77 mm. Initially, there is a spatial distance between the two cameras and the injected bubble. This is due to the linear unit drive being activated prior to the injection of a bubble, as discussed in Sec. IV C. Additionally, there are small variations in the needle detachment time. The bubble is therefore captured by camera I

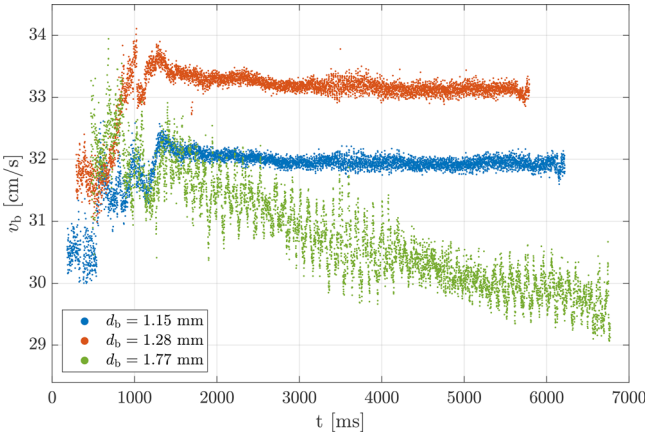

FIG. 13. Instantaneous bubble velocity vs rise time for bubbles of volume equivalent diameter $d_b = 1.15, 1.28, 1.77$ mm.

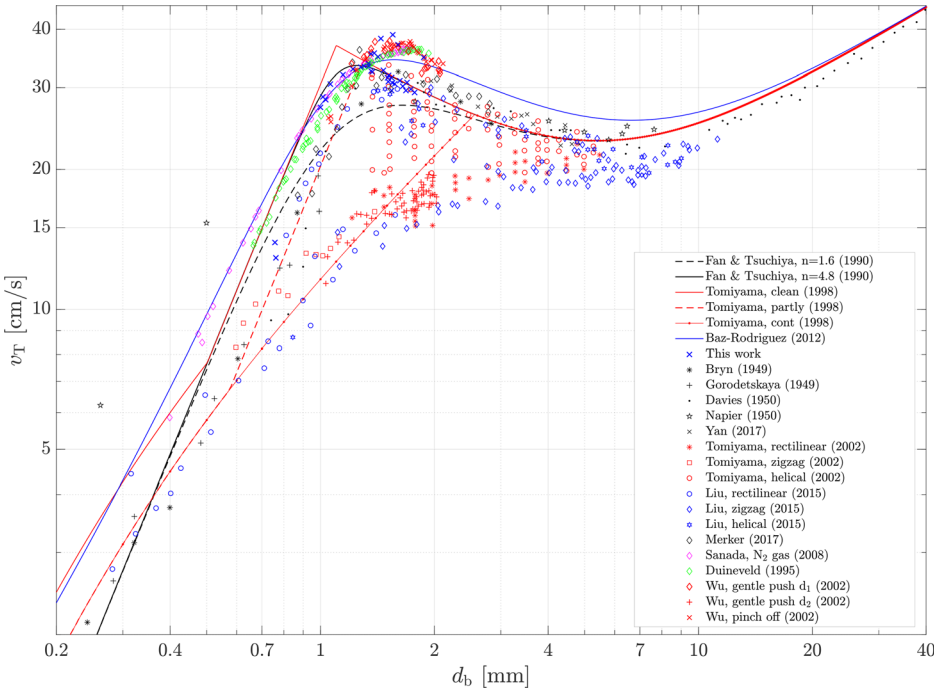

FIG. 14. Terminal velocity as function of bubble diameter, including experimental data and correlations found in the literature.

at $t > 0$, and the total bubble recording time varies for the individual bubble events. The bubbles with $d_b = 1.15$ and $d_b = 1.28$ mm in Fig. 13 are close to spherical in shape and rise in rectilinear paths. Due to the initial acceleration, the bubble velocities increase before reaching terminal values at approximately 1600 ms in both cases. As a result of the reduction in the hydrostatic pressure over the column height and a net-zero mass transfer, an increase in the bubble size is observed for all the bubble rise events. The ellipsoidal bubble of size $d_b = 1.77$ mm takes an oscillating rise path, resulting in a periodic fluctuating terminal velocity. Reflecting the increase in the bubble volume over the column, the amplitude of the path oscillations of $d_b = 1.77$ mm increases; hence, the terminal velocity decreases.

Including empirical data from the literature, Fig. 14 reveals a large scatter in the terminal velocities. As described in Sec. I A, the scatter has been attributed to both the purity of the liquid and the method of bubble formation. In the present work, a small scatter in the terminal velocities is observed for bubbles of comparable size. Comparing to the data by Tomiyama *et al.*,[18] Liu *et al.*,[25] and Wu and Gharib,[32] where bubbles have been produced by different methods, the small scatter in the present data indicates consistency in the method of bubble formation. This observation is of importance, as the needles are handmade and small variations in the design are unavoidable. With the inner diameter of the needle being smaller than the bubble diameter in all the experimental events, the bubbles are produced with large initial bubble shape deformations. For bubbles with a diameter smaller than the bubble formation device, the terminal velocity data obtained in this work coincide with the data by Tomiyama *et al.*,[18] Liu *et al.*,[25] and Wu and Gharib.[32] Second, the terminal velocities from the present work coincide with the data by Duineveld,[31] Sanada *et al.*,[22] and Wu and Gharib,[32] which have been obtained in ultra-purified water. This indicates that the de-ionized water employed in the present work can be regarded as pure.

As previously mentioned in Sec. II A, only the vertical bubble velocity component is considered when calculating the terminal

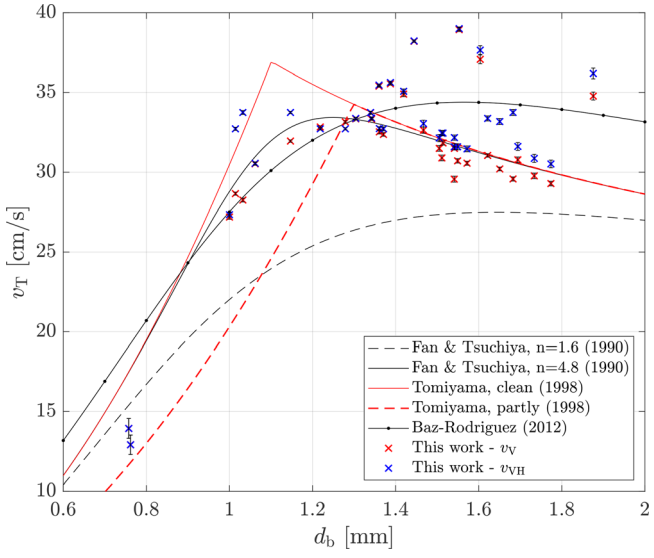

FIG. 15. Terminal velocity calculated by the vertical bubble velocity component, v_V, and the vertical and horizontal velocity component, v_{VH}, including the standard deviations and correlations found in the literature.

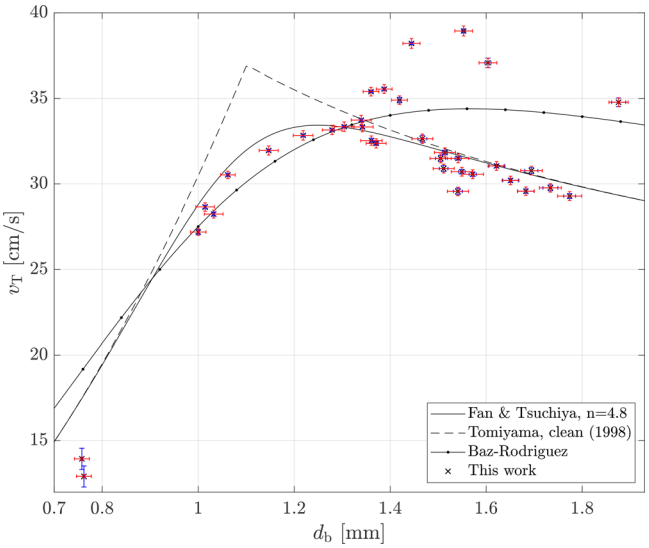

FIG. 16. Terminal velocity as function of bubble diameter, including experimental data, corresponding standard deviations, and correlations found in the literature. The standard deviations calculated from the propagation of error method are shown in red, and the standard deviations of the means are shown in blue.

velocity. Contradictory to most work reported in the literature, Liu *et al.*[25] and Yan *et al.*[26] (data are included in Fig. 14), considered both the vertical and the horizontal velocity components when calculating the terminal velocity. The different definitions used in the literature for the terminal velocity may contribute to the large data scatter in Fig. 14. Thus, to analyze the significance of including the horizontal velocity component in the calculation of the terminal velocity, both methods are considered in the present work and compared in Fig. 15. As expected, the terminal velocities calculated by the two methods are approximately equal for bubbles taking a rectilinear path. The onset to path oscillations is observed for bubbles in the size range $d_b \in [1.3, 1.56]$ mm, and thus, with increasing path oscillations, the influence of the horizontal velocity component becomes more significant which results in a larger terminal velocity than otherwise is obtained with the traditional definition of the terminal velocity. The maximum deviation between the two methods for computing the terminal velocity is 4% in the present work.

Figure 16 shows the terminal velocity as function of the bubble diameter, including the corresponding standard deviations, which have been calculated by both the propagation of error in Eq. (18) and the standard deviation of the mean in Eq. (B3). Comparing the uncertainties in Fig. 16, the two methods of calculation are seen to give close to equal values. This is in accordance with the textbook of Taylor.[55]

The minimum and maximum standard deviation of the mean, along with the terminal velocity and the bubble diameter, are given in Table VII. The deviation from the terminal velocity is in the range of [0.3, 4]%, and the deviation from the mean bubble diameter is in the range of [0.1, 1]%.

In three particular cases, specifically for $d_b = 1.44$, $d_b \in [1.55, 1.60]$, and $d_b = 1.88$ mm, the terminal velocities are considered to be high. Assessing the trajectories, a rectilinear rise path is observed for $d_b = 1.44$ mm, whereas oscillating rise paths are seen for $d_b \in [1.55, 1.60]$ and $d_b = 1.88$ mm. The calculated terminal velocities are based on 20, 10, and 12 bubble events, for $d_b = 1.44$, $d_b \in [1.55, 1.60]$, and $d_b = 1.88$ mm, respectively. Statistically, the three cases are found to be significant, shown by the low standard deviations in Fig. 16. In particular, for $d_b = 1.44$ mm, the standard deviation of the terminal velocity and the bubble diameter are 0.5 and 0.02, respectively. Assessing the original images and the calculated bubble properties reveals no obvious explanation for the relatively high values. At present, the higher data values are considered to be a result of the method of bubble formation.

TABLE VII. Minimum and maximum standard deviations of the mean along with the terminal velocity and the bubble diameter.

	Terminal velocity (cm/s)	Bubble diameter (mm)
Min	35.4 ± 0.1	1.000 ± 0.001
Max	13.9 ± 0.6	1.68 ± 0.02

TABLE VIII. Statistics of model performance on the terminal velocity, where the number of measurements $M = 35$.

	$d_b < 1.3$ mm			$d_b > 1.3$ mm			$d_b \in [0.76, 1.88]$ mm		
Correlation	ϵ	σ_e	c	ϵ	σ_e	c	ϵ	σ_e	c
Mendelson[16]	0.29	0.25	−0.98	0.05	0.07	0.24	0.11	0.17	−0.69
Fan, n = 1.6[36]	0.24	0.07	0.81	0.22	0.09	−0.34	0.23	0.09	−0.13
Fan, n = 4.8[36]	0.07	0.09	−0.89	0.05	0.07	0.24	0.06	0.08	−0.18
Jamialahmadi[45]	0.23	0.22	−0.97	0.06	0.08	0.26	0.10	0.15	−0.61
Baz-Rodriguez[23]	0.08	0.13	−0.85	0.07	0.04	0.68	0.07	0.07	−0.18
Tomiyama, clean[17]	0.13	0.07	−0.91	0.05	0.07	0.24	0.07	0.08	−0.39
Tomiyama, partly[17]	1.09	0.39	0.82	0.05	0.07	0.24	0.09	0.12	−0.50
Tomiyama, v = f(E)[18]	0.07	0.05	−0.69	0.06	0.08	0.22	0.06	0.07	−0.02

B. Analysis of correlations for the terminal velocity

The predictability of the correlations for the terminal velocity given in Tables III and IV was analyzed. This was done by comparing the relative error, e, the standard deviation of the error, σ_e, and the correlation factor, c, given by Eqs. (A1)–(A5) in Appendix A. In addition, the predictability was evaluated by using Figs. 22 and 23 in Appendix A, where the ratio of the predicted and the measured terminal velocity is plotted as a function of Eötvös number. The correlation factor, which indicates the strength of correlation between the experimental- and the correlation-based values, should be close to zero. A positive correlation factor indicates an overprediction, a negative correlation factor indicates an underprediction, whereas a zero-valued correlation factor indicates no linear relationship. Interpreted for this

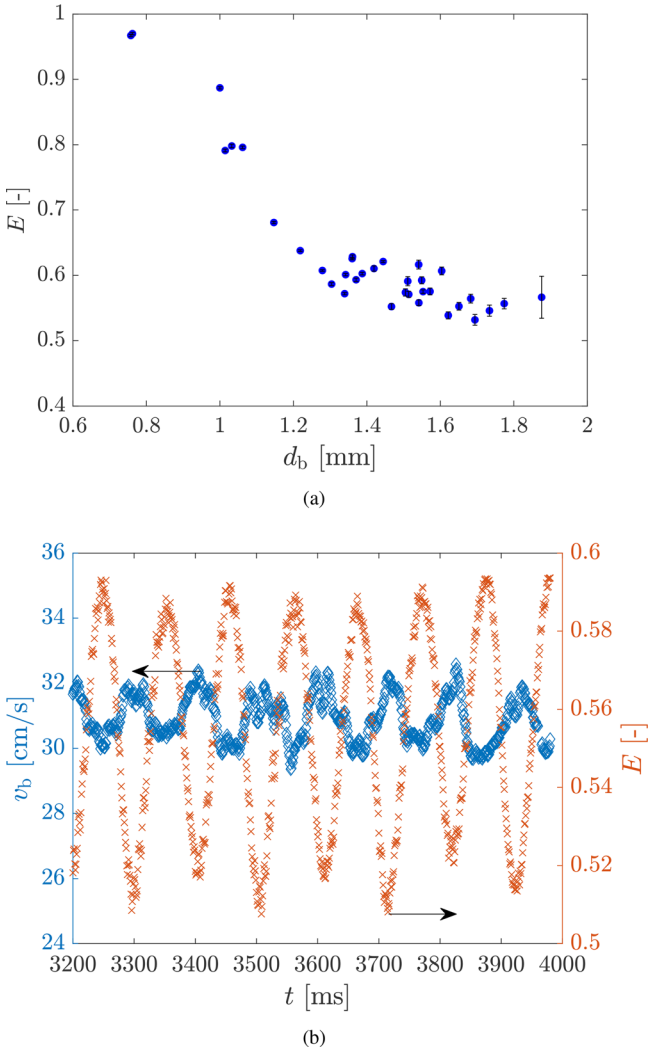

FIG. 17. (a) Bubble aspect ratio as function of bubble diameter, including standard deviations, (b) bubble velocity and aspect ratio as function of time for a bubble $d_b = 1.66$ mm.

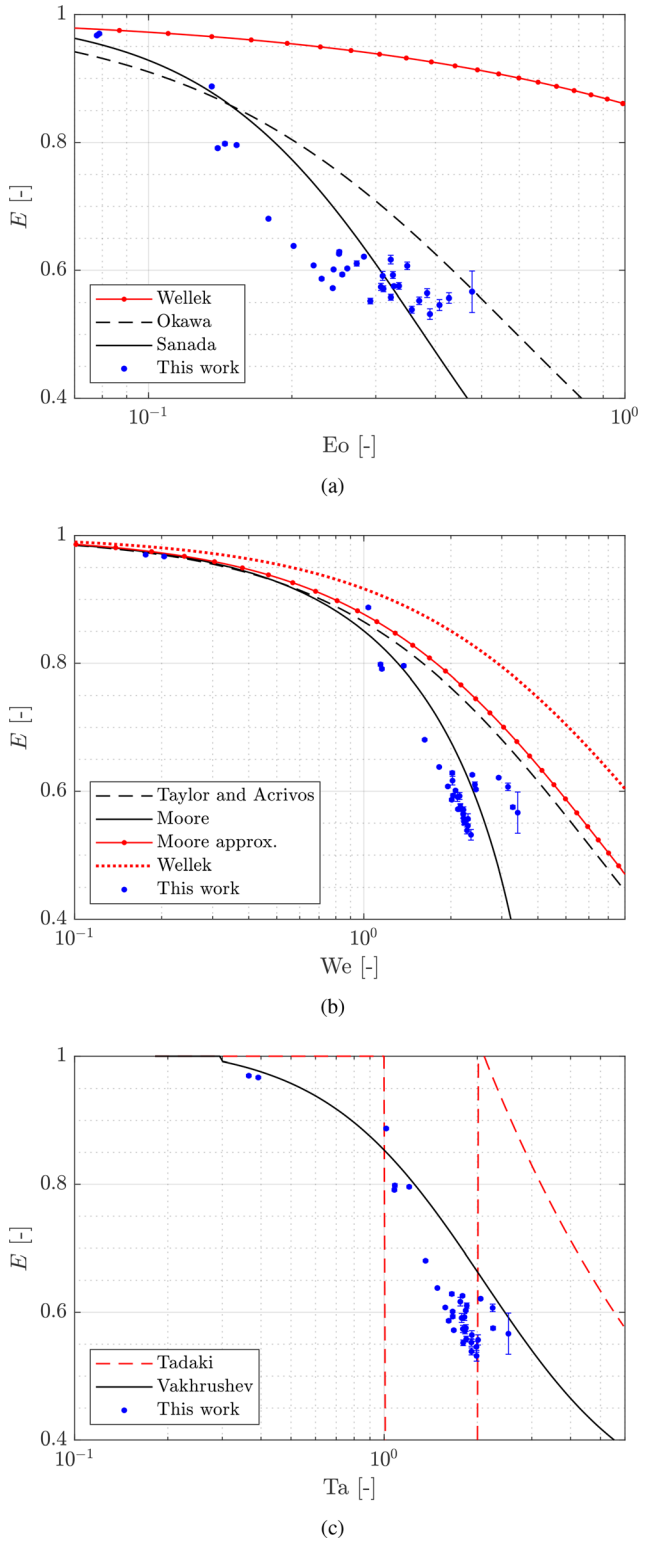

FIG. 18. Bubble aspect ratio as function of (a) Eötvos number, (b) Weber number, and (c) Tadaki number, including mean experimental values and available correlations.

specific case, a positive correlation factor indicates that the correlation tends to overpredict the experimental data with increasing bubble diameter, whereas the correlation tends to underpredict the data with decreasing bubble diameter. A negative correlation factor indicates the opposite. In Fig. 22, the correlation proposed by Mendelson[16] is seen to strongly overestimate the experimental data for Eo < 0.23. The correlation factor is $c = -0.98$. Statistical values of the correlations showing high predictability are given in Table VIII.

Large changes in the bubble dynamics are observed around the terminal velocity peak in Fig. 14. When validating correlations for the terminal velocity against experimental data, Celata *et al.*[21] suggested subdividing the evaluation into two size regions. Celata *et al.*[21] proposed the size regions $d_b < 1.3$ and $d_b > 1.3$ mm. The statistical values presented in Table VIII are calculated with and without subdividing the validation into the size regions suggested by Celata *et al.*[21] The number of experimental events used in the analysis is $M = 35$. Note that these values are average values based on N individual bubble rise events. Evaluating the bubbles with diameter $d_b < 1.3$ mm, the correlation by Tomiyama *et al.*,[18] given in Table III, gives the best prediction. The standard deviation and relative error when using the correlation by Tomiyama *et al.*[18] is $\sigma_e = 0.05$ and $\epsilon = 0.07$, respectively. The correlation by Fan and Tsuchiya[36] using n =4.8, given in Table III, predicts the experimental data well. The calculated standard deviation is $\sigma_e = 0.09$ and the relative error is $\epsilon = 0.07$. However, as seen in Fig. 22, the correlation by Fan and Tsuchiya[36] overestimates the data for Eo < 0.1.

For bubbles with diameter $d_b > 1.3$ mm, the correlations by Fan and Tsuchiya[36] (using n = 4.8), Tomiyama *et al.*,[17] Mendelson,[16] and Tomiyama *et al.*,[18] give good predictions. Except for a slightly higher correlation factor, the performance of the correlation proposed by Mendelson[16] is close to those by Fan and Tsuchiya,[36] Tomiyama *et al.*,[17] and Mendelson.[16] Regarding Figs. 22 and 23, the correlations by Fan and Tsuchiya,[36] Tomiyama *et al.*,[17] Mendelson,[16] Mendelson,[45] and Tomiyama *et al.*,[18] underestimate the same experimental data points. These data points are the high valued terminal velocities discussed in Sec. VII A.

The correlation by Tomiyama *et al.*[18] shows a high predictability when evaluating the experimental data without subdividing the evaluation into size regions. The statistical parameters when employing the correlation by Tomiyama *et al.*[18] were calculated to be $\sigma_e = 0.07$, $\epsilon = 0.06$, and $c = -0.02$.

C. Bubble aspect ratio

In Fig. 17(a), showing the bubble aspect ratio as a function of the bubble diameter, close to a linear decrease in the bubble aspect ratio is seen for $d_b < 1.3$ mm. Note that due to small values, some of the standard deviations plotted in Fig. 17(a) are not visible. For bubble diameter $d_b > 1.3$ mm, a spread in the bubble aspect ratio is observed. A similar trend was observed in the studies of Celata *et al.*,[21] Celata *et al.*,[20] and Liu *et al.*,[25] where a significant scatter in the bubble aspect ratio was observed for bubbles of size $d_b > 1$ mm. Reflecting the dynamic bubble behavior, Fig. 17(b) shows an inverse correlation between the instantaneous bubble velocity and the bubble aspect ratio for an oscillating bubble of size $d_b = 1.66$ mm. When the bubble velocity is high, the bubble aspect ratio is low, and vice versa. The observed dependency between the bubble velocity and aspect ratio confirms the earlier observations by Tomiyama *et al.*,[18] Celata *et al.*,[20,21] and Liu *et al.*[25]

The bubble aspect ratio was correlated as a function of the Eötvös, Weber, and Tadaki numbers. The correlations employed are

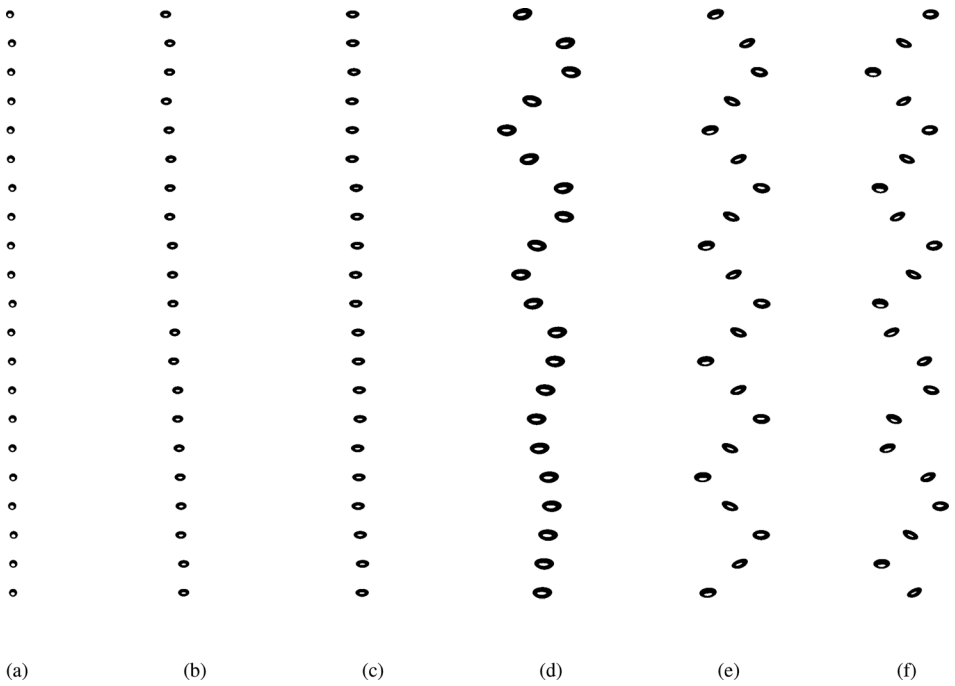

FIG. 19. Trajectory of various bubble sizes; (a) $d_b = 0.76$, (b) $d_b = 1.14$, (c) $d_b = 1.31$, (d) $d_b = 1.56$, (e) $d_b = 1.65$, and (f) $d_b = 1.75$ mm. Multimedia views: https://doi.org/10.1063/5.0061581.1; https://doi.org/10.1063/5.0061581.2; https://doi.org/10.1063/5.0061581.3; https://doi.org/10.1063/5.0061581.4; https://doi.org/10.1063/5.0061581.5; https://doi.org/10.1063/5.0061581.6

presented in Table V and Eqs. (4)–(6) in Sec. II. In Fig. 18(a), the data are correlated as a function of the Eötvös number. The bubble aspect ratio is seen to be overestimated by all the selected expressions for Eö ≤ 0.3, where the correlation by Wellek *et al.*[50] overestimates over the entire region. For $0.3 < \text{Eö} < 0.5$, the correlation proposed by Okawa *et al.*[19] serves as an upper boundary for the bubble aspect ratio, while the correlation of Sanada *et al.*[22]—as a lower boundary. Expressing the bubble aspect ratio in terms of the Weber number, the experimental data in Fig. 18(b) are less scattered compared to the data in Fig. 18(a). Except from the high values of the bubble aspect ratio around We =3, the correlation by Moore[49] gives a fairly good estimate of the bubble aspect ratio. Note that these high values of the bubble aspect ratio correspond to the high terminal velocities discussed in Sec. VII A. For Weber numbers We > 1 in Fig. 18(b), the correlations by Taylor and Acrivos[57] and Wellek *et al.*,[50] in addition to the approximated correlation by Moore,[49] are seen to overpredict the experimental data.

In Fig. 18(c), the bubble aspect ratio is expressed as function of the Tadaki number. For increasing Tadaki numbers, the correlation by Vakhrushev and Efremov,[52] given by Eq. (6), overestimates the data. The correlation by Tadaki and Maeda[51] in Eq. (5) clearly fails to predict the bubble aspect ratio in Fig. 18(c).

D. Bubble trajectory

Binarized image sequences of the bubble trajectories for bubbles with $d_b = 0.76$ to $d_b = 1.75$ mm are shown in Fig. 19 (Multimedia view). The time interval between two consecutive images in Fig. 19 is 50 ms. Note that the optical resolution employed is not equal for all the illustrations in Fig. 19. The spherical and ellipsoidal bubbles in Figs. 19(a)–19(c) rise in rectilinear paths. The bubble diameter at which path oscillations start to develop has been observed to vary in the present study, as discussed in Sec. VII A. Considering the influence

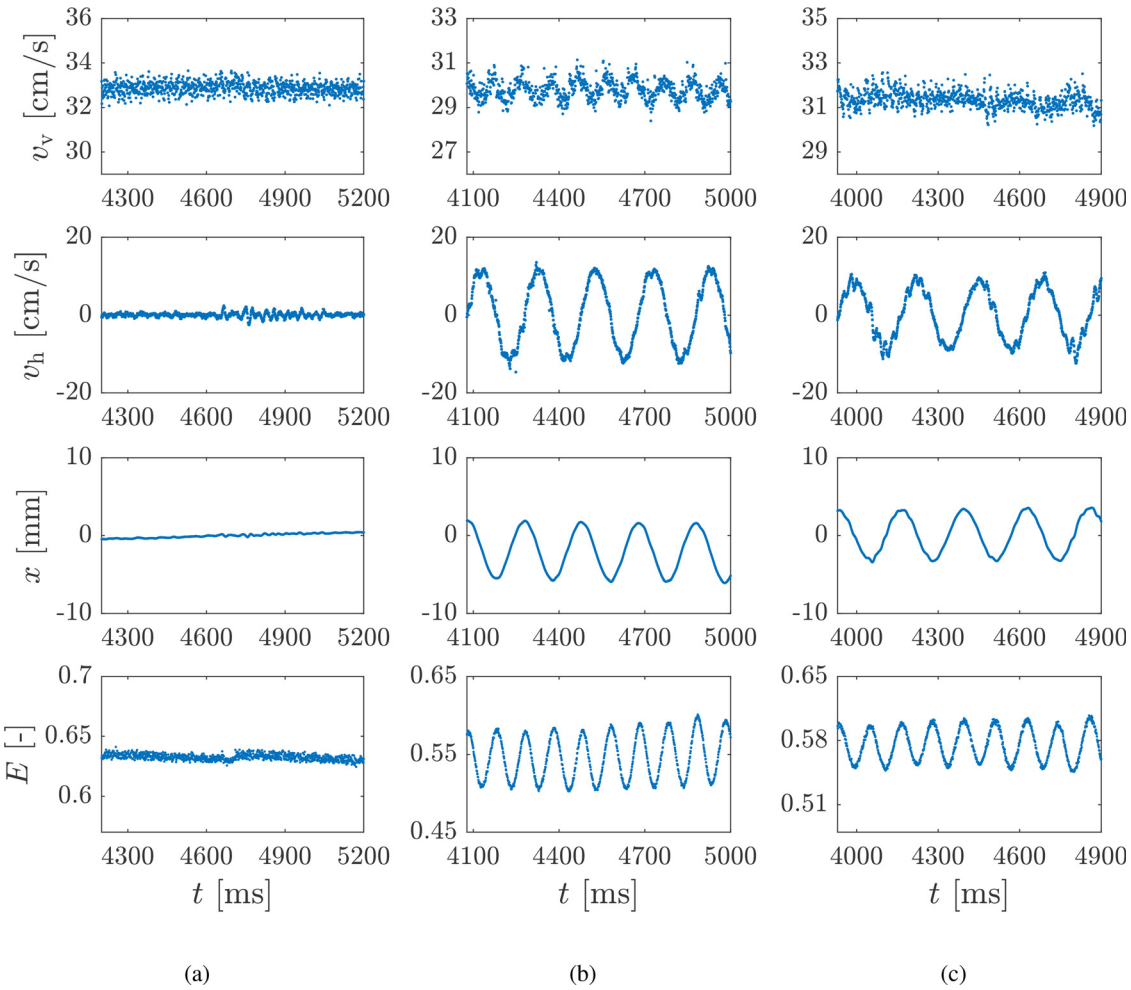

FIG. 20. Horizontal (v_h) and vertical (v_v) bubble velocity components, horizontal bubble position (x), and bubble aspect ratio (E) for a bubble with the following volume equivalent diameter and trajectory; (a) $d_b = 1.22$, rectilinear, (b) $d_b = 1.77$, zigzag, and (c) $d_b = 1.46$ mm, helical.

of the bubble formation method, a range in the bubble diameter of which path oscillations are initiated is to be expected. As the bubble diameter increases due to reduced hydrostatic pressure over the column height, the bubble in Fig. 19(d) reaches the onset to path oscillations during the ascent. The bubble motion changes from a rectilinear to an oscillating rise path. The path oscillations continue to develop as the bubble diameter further increases, as seen in Figs. 19(e) and 19(f). The frequency and amplitude of the path oscillations are dependent on the bubble diameter.

Analyzing the bubble velocity components and the horizontal bubble displacement (x-position), different rise paths can be distinguished based on the 2 D images. For a bubble rising with a rectilinear trajectory, as in Fig. 20(a), the path analysis is straightforward. The horizontal bubble velocity component, v_h, is zero or constant, and the vertical component, v_v, is flat. With no path oscillations, the deviation from the rise centerline is zero. In some cases, a steady movement from the centerline is observed. As noted by Celata *et al.*,[20] based on a force balance, this can only be explained by the action of a lift force. Being close to spherical, the bubble in Fig. 20(a) shows no bubble shape oscillations. Hence, the bubble aspect ratio is close to constant. A slightly steady decrease is observed, which reflects the increase in size due to the reduction in hydrostatic pressure.

In the study of Celata *et al.*[21] on the effect of injection method and liquid purity, single bubbles were studied from two directions by use of four mirrors and a single high-speed camera. Comparing the bubble data from single- and double-image acquisition, Celata *et al.*[21] found the largest deviation to be in contaminated water, with a maximum difference in the determined volume equivalent bubble diameter of approximately 2.3%. In pure water, the maximum difference in calculated bubble diameter was 0.3%. Celata *et al.*[21] differentiated between a zigzag and a helical rise path based on the position and velocity components of the two projections. The observations of the velocity components and the bubble position in the present study are in accordance with the analysis of Celata *et al.*[21] In Fig. 20(b), a bubble rising in a zigzag path is shown. v_v reaches a maximum when x is at its maximum or minimum, i.e., when the bubble changes the horizontal direction. When the bubble is at the center, i.e., $x = 0$, v_v reaches a minimum value and the horizontal velocity component, v_h, is at a maximum. v_v is seen to oscillate with twice the frequency of v_h and x. It is not possible to distinguish between a zigzag and helical trajectory based on the evaluation of v_h and x from 2D images. In both cases, oscillations are observed in v_h and x. Evaluating helical rising bubbles, Celata *et al.*[21] observed v_v to be close to constant, contrary to the oscillating component for a zigzag rise path. Celata *et al.*[21] noted that for a helical rising bubble, v_h and x will oscillate in and out of phase of 90°. Analyzing the bubble in Fig. 20(c), v_v is seen to be close to constant, where v_h and x are oscillating out of phase close to 90°. It can be concluded that the bubble in Fig. 20(c) takes a helical rise path.

The bubble aspect ratio, which is strongly correlated with the bubble velocity, is seen to oscillate for both the zigzag and helical trajectory.

E. Statistical treatment

Continuous data acquisition of a single bubble over a longer spatial distance may be extremely time-demanding. Statistical accuracy is often related to a high number of experimental repetitions. To limit the number of experimental events, while ensuring a high level of accuracy, the standard deviation and the confidence interval of a measured quantity could be evaluated for an increased number of executions. Figure 21 shows the terminal velocity vs the number of experimental events for bubbles with a mean diameter $d_b = 1.34$ mm. The standard deviation is seen to be small and approaching a constant value after only five bubble rise events. As the confidence interval only depends on the standard deviation and the number of experimental events, a decrease in the confidence interval is to be expected when the standard deviation approaches a constant value. The decrease is then depending on the factor $(N-1)^{-1/2}$, which has a minor effect on the confidence interval as $(N-1)^{-1/2} = 0.23$ and $(N-1)^{-1/2} = 0.19$ for $N = 20$ and $N = 30$, respectively. Thus, the value of operating hours vs the small effect on the confidence level by performing additional experiments should be considered. Evaluating all the experimental events, the number of necessary bubble rise events is found to be 10–15.

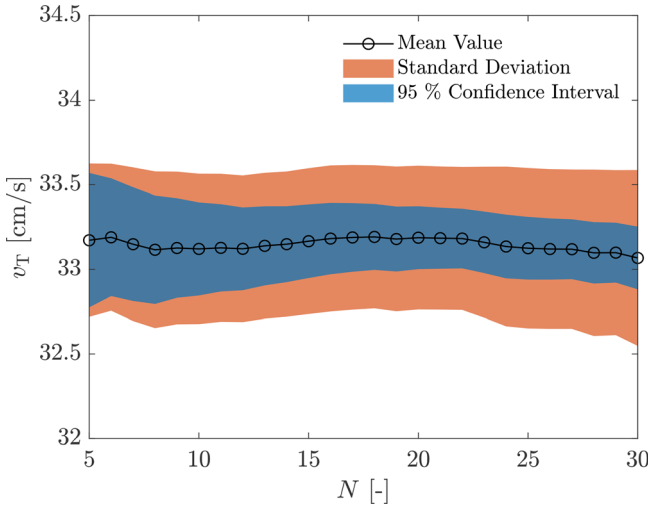

FIG. 21. Terminal velocity vs number of bubble rise events for bubbles with mean diameter $d_b = 1.34$ mm, including the standard deviation and the 95% confidence interval.

VIII. CONCLUDING REMARKS

Single air bubbles rising in a vertical column containing stagnant de-ionized water have been evaluated based on an image analysis technique. The implementation of two high-speed cameras on a linear unit drive allowed for continuous evaluation of the bubble velocity, size, and trajectory as the bubbles ascend through the column. Glass needles were employed for bubble formation of which the inner diameter never exceeded that of the volume equivalent diameter of the produced bubble. Hence, all the bubbles were injected with initially large shape deformations. For comparable bubble size, the measured terminal velocities coincide with the higher terminal velocities reported in the literature. This confirms earlier observations by Tomiyama *et al.*,[18] which stated that initially large shape deformations will result in higher

terminal velocities. The statistically significant terminal velocities obtained in this work are less scattered compared to the existing data presented in the literature.

Regarding the bubble trajectory, bubbles with a volume equivalent diameter of $d_b < 1.3$ mm, are observed to rise in a rectilinear path. In some cases, the bubbles rise in a rectilinear path with a steady movement from the centerline. The presence of a novel lift force in the initial axisymmetric configuration has been proposed in the literature. A symmetry breaking bifurcation which could explain such behavior has been mentioned in the review by Shi and Rzehak.[58] Path oscillations are seen to be initiated for bubbles in the size range $d_b \in [1.3, 1.56]$ mm. For bubbles rising with path oscillations, the instantaneous bubble velocity and bubble aspect ratio are inversely correlated. This means that when the bubble velocity is high, the bubble aspect ratio is low, and vice versa. Due to the bubble volume expansion with reduced hydrostatic pressure along the column height, the movement in the horizontal direction increases for bubbles taking an oscillating rise path. A transition from an initially rectilinear rise path to a zigzag or a helical is observed for several bubble events, reaching an onset to oscillations during rise due to the increasing bubble volume.

The existing correlations for the terminal velocity are validated against the experimental data obtained in this work. The best prediction of the experimental data is given by the correlation proposed by Tomiyama *et al.*[18] Correlated in terms of dimensionless groups, the bubble aspect ratio is well predicted when correlated as function of the Weber number. The best prediction was given by the correlation suggested by Moore.[49]

A thorough statistical analysis has been presented. The random uncertainties in the experimental data have been calculated by the propagation of error formula and the standard deviation of the mean. The two methods gave approximately the same values for the standard deviation. The statistical significance of the experimental data has been quantified. For the terminal velocity, the percentage deviation from the mean is in the range of [0.3, 4]%. The percentage deviation from the mean bubble diameter ranges from [0.1, 1]%.

The number of experimental events necessary to obtain high precision data has been evaluated using a 95% confidence interval. In this work, high statistical precision is obtained after 10–15 bubble rise events. Considering time efficiency, increasing the number of experimental repetitions to increase the accuracy of the data is not desirable. Covering a wider bubble size range of high precision bubble data, explicitly reporting on the bubble formation method, should be prioritized.

In summary, the statistically significant terminal velocity data obtained in this work show a small scatter compared to existing data in the literature. The bubbles, which were produced with initial large shape deformations, coincide with the higher terminal velocities reported in the literature. The continuous tracking of the bubbles over a tall vertical column allows for studying the effect of hydrostatic pressure on the bubble motion and size. Several bubbles initially rising in a rectilinear rise path were observed to initiate path oscillations as the bubble size increased due to reduced hydrostatic pressure. A thorough statistical analysis has been presented where the experimental uncertainties have been calculated based on different statistical methods. Important parameters involved in the image analysis have been evaluated, and the importance of the choice of threshold value used in the binarization of the raw images has been illustrated and quantified. The presented statistical analysis can benefit future work on single bubbles, as it could serve as a basis to increase the statistical accuracy of the experimental data.

APPENDIX A: STATISTICAL ANALYSIS OF TERMINAL VELOCITY CORRELATIONS

The correlations for the terminal velocity presented in Tables III and IV in Sec. II have been evaluated against the experimental data obtained in this work. In the following, the equations employed to statistically evaluate the predictability of the correlations are given.

The relative error between the experimental and the predicted terminal velocity is calculated by

$$e = \frac{v_{exp} - v_{cal}}{v_{cal}}, \tag{A1}$$

where v_{exp} and v_{cal} are the experimental and model predicted values, respectively.

The standard deviation of the error is

$$\sigma_e = \sqrt{\frac{\sum_{i=1}^{M} (e_i - \epsilon)^2}{M - 1}}, \tag{A2}$$

where M is the number of measurements (averaged values of N individual bubble rise events) and ϵ is the mean error of e:

$$\epsilon = \frac{1}{M} \sum_{i=1}^{M} e_i. \tag{A3}$$

The correlation factor $c \in [-1, 1]$ is given by

$$c = \frac{\mathrm{Cov}(e, d)}{\sigma_e \sigma_d} = \frac{\sum_{i=1}^{M} (e_i - \epsilon)(d_{b,i} - \overline{d_b})}{\sqrt{\sum_{i=1}^{M} (e_i - \epsilon)^2} \sqrt{\sum_{i=1}^{M} (d_{b,i} - \overline{d_b})^2}}, \tag{A4}$$

where σ_d and $\overline{d_b}$ are the standard deviation and the mean value of the bubble diameter, respectively.

$\mathrm{Cov}(e, d)$ is the covariance of e and d,

$$\mathrm{Cov}(e, d) = \frac{\sum_{i=1}^{M} (e_i - \epsilon)(d_{b,i} - \overline{d_b})}{M - 1}. \tag{A5}$$

Figure 22 shows the ratio between the estimated and measured terminal velocity as function of the Eötvös number.

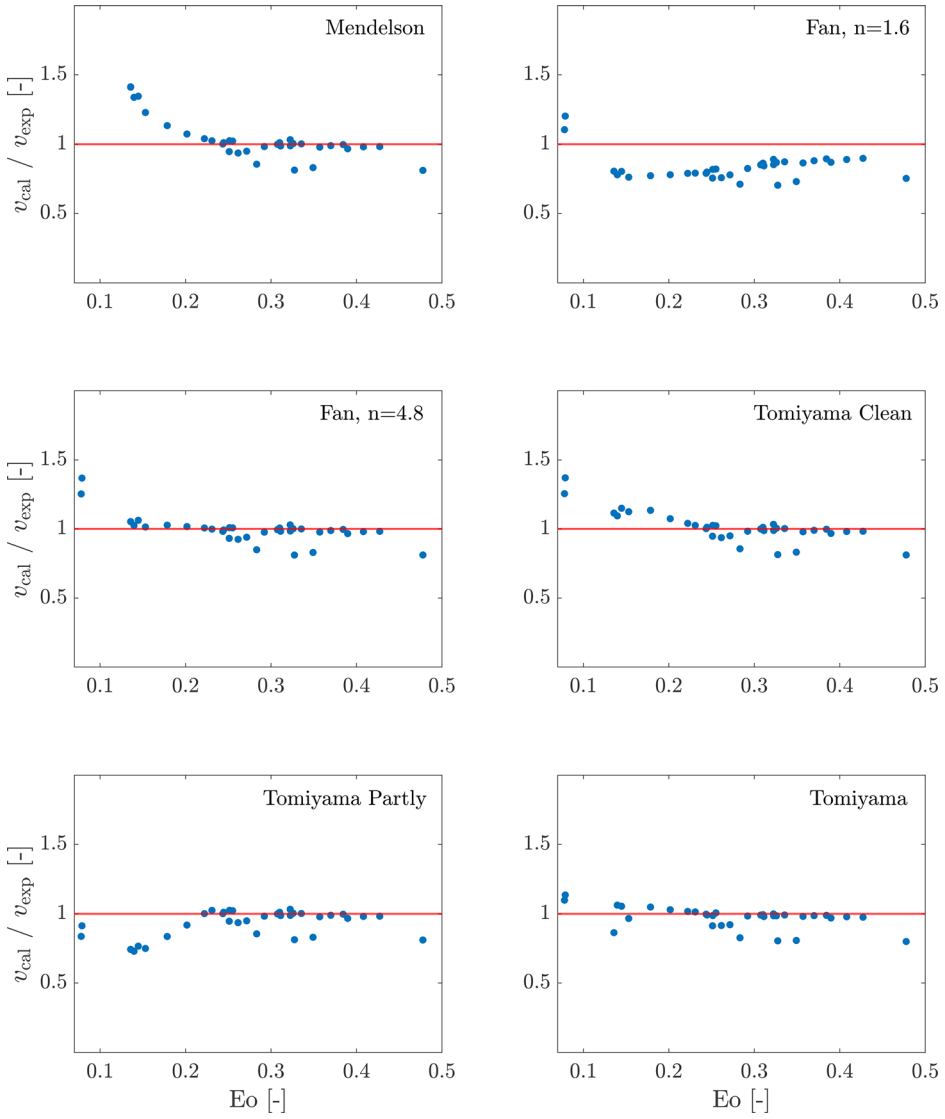

FIG. 22. a) Ratio of the predicted and measured terminal velocity as function of Eötvös number (see correlations in Tables III and IV).

APPENDIX B: STATISTICAL ANALYSIS—REPEAT OF MEASUREMENTS

The mean, $\bar{x}$, and the sample standard deviation, S, can be calculated by the general formulas[55]

$$\bar{x} = \frac{\sum_{i=1}^{N} x_i}{N}, \tag{B1}$$

$$S = \left(\frac{\sum_{i=1}^{N} (x_i - \bar{x})^2}{N-1} \right)^{1/2}, \tag{B2}$$

where x_i is the specific quantity calculated for a single bubble event, and N denotes the number of bubble rise events.

The standard deviation of the mean is given by Eq. (B3):

$$\bar{S} = \frac{S}{\sqrt{N}}. \tag{B3}$$

The $1-\alpha$ confidence interval for the true mean, μ, can be calculated by Eq. (B4).

$$\bar{x} \pm t_{n-1,\alpha/2}\bar{S}, \tag{B4}$$

where $t_{n-1,\alpha/2}$ denotes the size of the confidence interval.

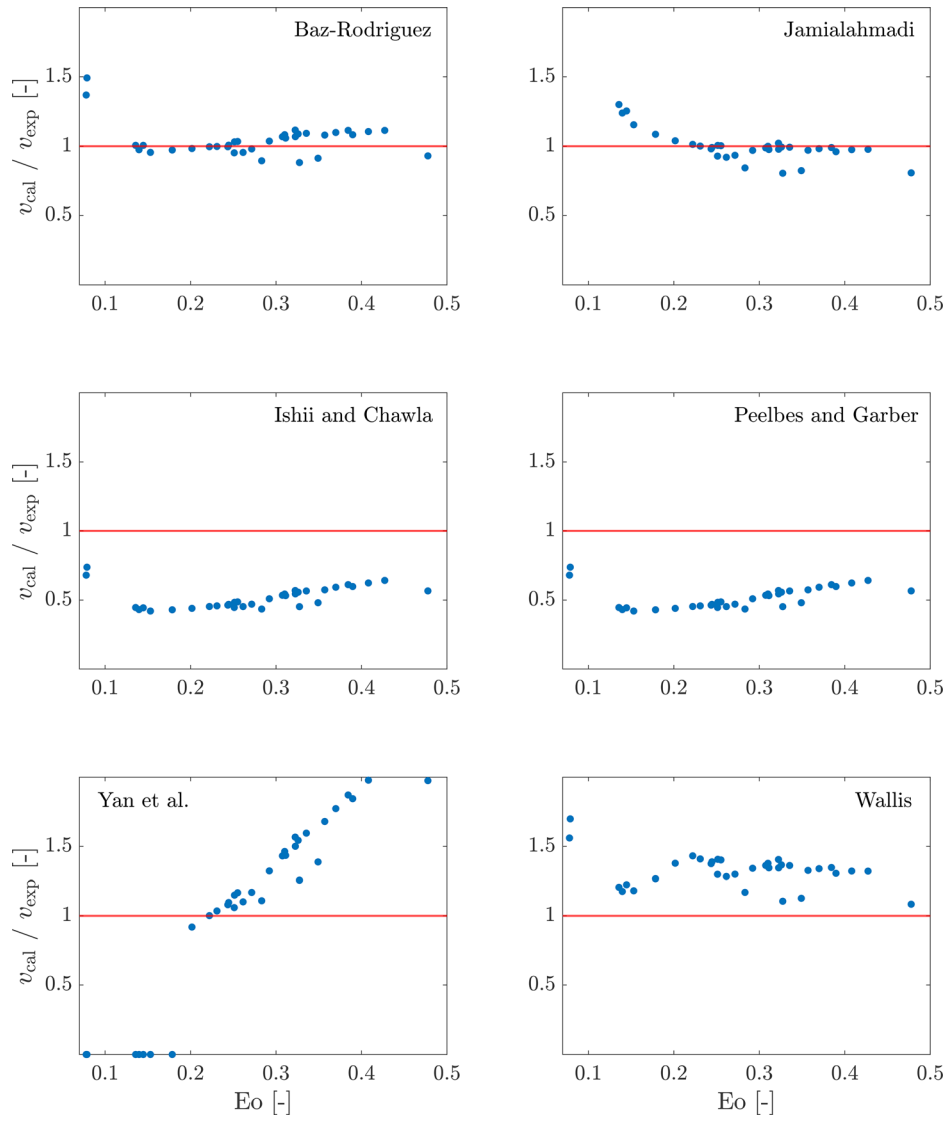

FIG. 22. b) Ratio of the predicted and measured terminal velocity as function of Eötvös number (see correlations in Tables III and IV).

APPENDIX C: STATISTICAL ANALYSIS—PROPAGATION OF ERRORS

The partial derivatives applied to calculate the uncertainty in the terminal velocity are given by

$$\frac{\partial v_b}{\partial P_{ybar,k+1}} = \frac{h_{\mathrm{cal,m}}}{h_{\mathrm{cal,px}}}\frac{1}{\Delta t}, \tag{C1}$$

$$\frac{\partial v_b}{\partial h_{\mathrm{cal,m}}} = \frac{1}{h_{\mathrm{cal,px}}}\frac{\Delta P_{\mathrm{ybar}} - \Delta P_{\mathrm{yb}}}{\Delta t}, \tag{C2}$$

$$\frac{\partial v_b}{\partial h_{\mathrm{cal,px}}} = -\frac{h_{\mathrm{cal,m}}}{h^2_{\mathrm{cal,px}}}\frac{\Delta P_{\mathrm{ybar}} - \Delta P_{\mathrm{yb}}}{\Delta t}, \tag{C3}$$

$$\frac{\partial v_b}{\partial \Delta t} = -\frac{h_{\mathrm{cal,m}}}{h_{\mathrm{cal,px}}}\frac{\Delta P_{\mathrm{ybar}} - \Delta P_{\mathrm{yb}}}{\Delta t^2}. \tag{C4}$$

In addition, $\partial v_{\mathrm{b}}/\partial P_{\mathrm{ybar,k+1}} = -\partial v_{\mathrm{b}}/\partial P_{\mathrm{ybar,k}} = -\partial v_{\mathrm{b}}/\partial P_{\mathrm{yb,k+1}} = \partial v_{\mathrm{b}}/\partial P_{\mathrm{yb,k}}$.

The partial derivatives used to calculate the uncertainty in the bubble diameter are given by

$$\frac{\partial d_{\mathrm{b}}}{\partial A} = \frac{1}{3}B^2\left(\frac{h_{cal,m}}{h_{cal,px}}\right)^3\left[\left(\frac{h_{cal,m}}{h_{cal,px}}\right)^3 AB^2\right]^{-2/3}, \tag{C5}$$

$$\frac{\partial d_{\mathrm{b}}}{\partial B} = \frac{2}{3}AB\left(\frac{h_{cal,m}}{h_{cal,px}}\right)^3\left[\left(\frac{h_{cal,m}}{h_{cal,px}}\right)^3 AB^2\right]^{-2/3}, \tag{C6}$$

$$\frac{\partial d_b}{\partial h_{cal,m}} = \frac{h_{cal,m}^2}{h_{cal,px}^3} AB^2 \left[\left(\frac{h_{cal,m}}{h_{cal,px}} \right)^3 AB^2 \right]^{-2/3}, \tag{C7}$$

$$\frac{\partial d_b}{\partial h_{cal,px}} = -\frac{h_{cal,m}^3}{h_{cal,px}^4} AB^2 \left[\left(\frac{h_{cal,m}}{h_{cal,px}} \right)^3 AB^2 \right]^{-2/3}. \tag{C8}$$

DATA AVAILABILITY

The data that support the findings of this study are available from the corresponding author upon reasonable request.

REFERENCES

[1]B. H. Hjertager, "Computational fluid dynamics (CFD) analysis of multiphase reactors," Trends Chem. Eng. **4**, 45–92 (1998).
[2]H. A. Jakobsen, "Modeling of vertical bubble-driven flows," Ind. Eng. Chem. Res. **36**, 4052–4074 (1997).
[3]H. A. Jakobsen, *Chemical Reactor Modeling: Multiphase Reactive Flows*, 2nd ed. (Springer, Berlin, 2014), Vol. 1.
[4]P. M. Doran, *Bioprocess Engineering Principles*, 2nd ed. (Elsevier Ltd., 2013).
[5]V. Cappello, C. Plais, C. Vial, and F. Augier, "Bubble size and liquid-side mass transfer coefficient measurements in aerated stirred tank reactors with non-Newtonian liquids," Chem. Eng. Sci. **211**, 115280 (2020).
[6]R. T. Lahey, Jr., "The analysis of phase separation and phase distribution phenomena using two-fluid models," Nucl. Eng. Des. **122**, 17–40 (1990).
[7]R. T. Lahey, Jr., "The simulation of multidimensional multiphase flows," Nucl. Eng. Des. **235**, 1043–1060 (2005).
[8]T. Haas, C. Schubert, M. Eickhoff, and H. Pfeifer, "A review of bubble dynamics in liquid metals," Metals **11**, 664–646 (2021).
[9]G. Stokes, "On the effect of the internal friction of fluids on the motion of pendulums," Trans. Cambridge Philos. Soc. **9**, 8–27 (1851).
[10]V. Levich, *Physicochemical Hydrodynamics* (Prentice-Hall, Englewood Cliffs, NJ, 1962); cited in Ref. 36.
[11]J. Hadamard, "Mouvement permanent lent d'une sphere liquide et visqueuse dans un liquide visqueux," C. R. Acad. Sci. Paris **152**, 1735–1738 (1911).
[12]W. Rybczynski, "Über die fortschreitende bewegung einer flüssigen kugel in einem zähen medium," Bull. Int. Acad. Sci. Cracovie **1**, 40–46 (1911).
[13]F. Peebles and H. Garber, "Studies on the motion of gas bubbles in liquids," Chem. Eng. Sci. **49**, 88–97 (1953).
[14]W. Haberman and R. Morton, "An experimental study of bubbles moving in liquids," Trans. Am. Soc. Civil Eng. **121**, 227–250 (1956).
[15]W. Haberman and R. Morton, "An experimental investigation of the drag and shape of air bubbles rising in various liquids," Trans. Am. Soc. Civil Eng. **802**, 227–250 (1953).
[16]H. Mendelson, "The prediction of bubble terminal velocities from wave theory," AIChE J. **13**, 250–253 (1967).
[17]A. Tomiyama, I. Kataoka, I. Zun, and T. Sakaguchi, "Drag coefficients of single bubbles under normal and micro gravity conditions," JSME Int. J. **41**, 472–479 (1998).
[18]A. Tomiyama, G. Celata, S. Hosokawa, and S. Yoshida, "Terminal velocity of single bubbles in surface tension force dominant regime," Int. J. Multiphase Flow **28**, 1497–1519 (2002).
[19]T. Okawa, T. Tanaka, I. Kataoka, and M. Mori, "Temperature effect on single bubble rise characteristics in stagnant distilled water," Int. J. Heat Mass Transfer **46**, 903–931 (2003).
[20]G. Celata, F. D'Annibale, P. D. Marco, G. Memoli, and A. Tomiyama, "Measurements of rising velocity of a small bubble in a stagnant fluid in one- and two-component systems," Exp. Therm. Fluid Sci. **31**, 609–623 (2007).
[21]G. Celata, M. Cumo, F. D'Annibale, P. D. Marco, A. Tomiyama, and C. Zovini, "Effect of gas injection mode and purity of liquid on bubble rising in two-component systems," Exp. Therm. Fluid Sci. **31**, 37–53 (2006).
[22]T. Sanada, K. Sugihara, M. Shirota, and M. Watanabe, "Motion and drag of a single bubble in a super-purified water," Fluid Dyn. Res. **40**, 534–545 (2008).
[23]S. Baz-Rodrígues, A. Aguilar-Corona, and A. Soria, "Rising velocity for single bubbles in pure liquids," Rev. Mex. Ing. Quím. **11**, 269–278 (2012).
[24]L. Liu, H. Yan, G. Zhao, and J. Zhuang, "Experimental studies on the terminal velocity of air bubbles in water and glycerol aqueous solution," Exp. Therm. Fluid Sci. **78**, 254–265 (2016).
[25]L. Liu, H. Yan, and G. Zhao, "Experimental studies on the shape and motion of air bubbles in viscous liquids," Exp. Therm. Fluid Sci. **62**, 109–121 (2015).
[26]X. Yan, Y. Jia, L. Wang, and Y. Cao, "Drag coefficient fluctuation prediction of a single bubble rising in water," Chem. Eng. J. **316**, 553–562 (2017).
[27]R. M. Davies and G. Taylor, "The mechanics of large bubbles rising through extended liquids and through liquids in tubes," Proc. R. Soc. London A **200**, 375–390 (1950).
[28]R. Clift, J. Grace, and M. Weber, *Bubbles, Drops, and Particles* (Academic Press, NY, 1978).
[29]N. Aybers and A. Tapucu, "The motion of gas bubbles rising through stagnant liquid," Wärme- und Stoffübertragung **2**, 118–128 (1969).
[30]S. Alves, S. Orvalho, and J. Vasconcelos, "Effect of bubble contamination on rise velocity and mass transfer," Chem. Eng. Sci. **60**, 1–9 (2005).
[31]P. Duineveld, "The rise velocity and shape of bubbles in pure water at high Reynolds number," J. Fluid Mech. **292**, 325–332 (1995).
[32]M. Wu and M. Gharib, "Experimental studies on the shape and path of small air bubbles rising in clean water," Phys. Fluids **14**, 49–52 (2002).
[33]D. Merker, L. Böhm, M. Oberger, P. Klüfers, and M. Kraume, "Mass transfer in reactive bubbly flows—A single bubble study," Chem. Eng. Technol. **40**, 1391–1399 (2017).
[34]M. Ishii and T. Chawla, Local drag laws in dispersed two-phase flow, Report No. ANL-79-105, 1979.
[35]J. Solsvik, "Lagrangian modeling of mass transfer from a single bubble rising in a stagnant liquid," Chem. Eng. Sci. **190**, 370–383 (2018).
[36]L. Fan and K. Tsuchiya, *Bubble Wake Dynamics in Liquids and Liquid-Solid Suspensions* (Butterworth-Heinemann, 1990).
[37]R. M. Griffith, "The effect of surfactants on the terminal velocity of drops and bubbles," Chem. Eng. Sci. **17**, 1057–1070 (1962).
[38]A. Frumkin and V. Levich, "On surfactants and interfacial motion," Zh. Fiz. Khim. **21**, 1183–1204 (1947); cited in Ref. 37.
[39]P. Saffman, "On the rise of small air bubbles in water," J. Fluid Mech. **1**, 249–275 (1956); cited in Ref. 40.
[40]K. Ellingsen and F. Risso, "On the rise of an ellipsoidal bubble in water: Oscillatory paths and liquid-induced velocity," J. Fluid Mech. **440**, 235–268 (2001).
[41]T. Bryn, "Speed of rise of air bubbles in liquids," Report No. 132, David Taylor Model Basin, 1949; cited in Ref. 28.
[42]A. Gorodetskaya, "The rate of rise of bubbles in water and aqueous solutions at great Reynolds numbers," Zh. Fiz. Khim. **23**, 71–77 (1949); cited in Ref. 28.
[43]R. M. Davies and G. I. Taylor, "The mechanics of large bubbles rising through extended liquids in tubes," Proc. R. Soc. A **200**, 375–390 (1950); cited in Ref. 28.
[44]R. L. Datta, D. H. Napier, and D. M. Newitt, "The properties and behaviour of gas bubbles formed at a circular orifice," Trans. Inst. Chem. Eng. **28**, 14–26 (1950); cited in Ref. 28.
[45]M. Jamialahmadi and H. Müller-Steinhagen, "Effect of superficial gas velocity on bubble size, terminal bubble rise velocity and gas hold-up in bubble columns," Dev. Chem. Eng. **1**, 16–31 (2008).
[46]R. Mei and J. F. Klausner, "Unsteady force on a spherical bubble at finite Reynolds number with small fluctuations in the free-stream velocity," Phys. Fluids A **4**, 63–70 (1992).
[47]L. Schiller and Z. Naumann, "A drag coefficient correlation," Z. Ver. Dtsch. Ing. **77**, 318–323 (1935).
[48]A. Tomiyama, A. Yoshida, and S. Hosokawa, "Surface tension force dominant regime of single bubbles rising through stagnant liquids," on *CD-ROM of 4th UK-Japan Seminar on Multiphase Flow, Bury St. Edmunds, UK* (2001), pp. 1–6; cited in Ref. 21.
[49]D. Moore, "The rise of a gas bubble in a viscous liquid," J. Fluid Mech. **6**, 113–130 (1959).
[50]R. Wellek, A. Agrawal, and A. Skelland, "Shape of liquid drops moving in liquid media," AIChE J. **12**, 854–862 (1966).
[51]T. Tadaki and S. Maeda, "On the shape and velocity of single air bubbles rising in various liquids," Chem. Eng. **25**, 254–264 (1961); cited in Ref. 20.

[52]I. Vakhrushev, G. Efremov *et al.*, "Interpolation formula for computing the velocities of single gas bubbles in liquids," Chem. Technol. Fuels Oils **6**, 376–379 (1970); cited in Ref. 28.
[53]C. C. M. E. Al-Mualla and D. Bull, *Video Coding for Mobile Communications* (Academic Press, 2001).
[54]N. Otsu, "A treshold selection method from gray-level histograms," IEEE Trans. Syst., Man Cybern. **9**, 62–66 (1979).
[55]J. Taylor, *An Introduction to Error Analysis* (University Science Books, 1997).
[56]W. Navidi, *Statistics for Engineers and Scientists*, 2nd ed. (McGraw-Hill International Edition, 2008).
[57]T. Taylor and A. Acrivos, "On the deformation and drag of a falling viscous drop at low Reynolds number," J. Fluid Mech. **18**, 466–476 (1964).
[58]P. Shi and R. Rzehak, "Lift forces on solid spherical particles in unbounded flows," Chem. Eng. Sci. **208**, 115145 (2019).